Chapter 5

Distribution of Particulates in the Tropical UTLS over the Asian Summer Monsoon Region and Its Association with Atmospheric Dynamics

S.V. Sunilkumar, K. Parameswaran and Bijoy V. Thampi

Additional information is available at the end of the chapter

http://dx.doi.org/10.5772/50552

1. Introduction

Particulates in the Upper Troposphere and Lower Stratosphere (UTLS) gained considerable interest due to their role in the dehydration of tropospheric air entering the stratosphere [1,2] as well as their potential to influence the radiation budget of the Earth-atmosphere system [3]. The upper troposphere region, which is also conducive for the formation of cirrus, plays a major role in the transport of water vapour and other chemical constituents into the stratosphere. The physical processes responsible for maintaining the observed aerosol distribution in the tropical UTLS, the process with which it interacts with cirrus clouds and the effect of these particulates on the radiation budget are not fully understood [4]. Studies have shown that the microphysical (such as particle shape, size, and size distribution) as well as the chemical properties of particles in the UTLS region [5-7] are mainly governed by the strength of tropospheric convection and the prevailing dynamics of the underlying troposphere. The formation and persistence of cirrus clouds in the upper troposphere is mainly governed by the concentration of available condensation nuclei in this region and their physical and chemical properties. These clouds are believed to be a significant contributor to atmospheric greenhouse effect [8,9] as well as hypothesized to play a major role in the dehydration of the lower stratosphere [1,2] and thus becomes an important factor governing global climate, through their positive feedback.

The last four decades of the 20th century have been marked by relatively intense volcanic activity [10] and hence long-term measurements of aerosols during this period mostly characterize the volcanically perturbed aerosols system rather than 'background' conditions [11-13]. During this period the increase in aerosol loading in the stratosphere could accelerate the heterogeneous chemistry of sulfate aerosols leading to a decrease in ozone amount [14-17], altering the NO_2 concentration [18-20] and hence modifying the earth's

radiation budget [21]. However, long-term studies on stratospheric aerosols show that on a global scale the stratospheric aerosol loading has returned to the pre-eruption levels (prevailed in the late 1970s) after the eruption of Mt. Pinatubo in 1991 [13,22] for the first time in 1998 and continued to remain almost at the same level for a couple of years. Only very few studies are carried out on the characteristics of these background stratospheric aerosols using observational data [7,13,23]. These studies, however, have shown that the global distribution of stratospheric aerosols will be significantly influenced by the atmospheric dynamics which includes periodic variations, such as the Quasi-Biennial Oscillation (QBO), seasonal cycles and long-term secular changes in addition to small perturbations due to the feeble volcanic eruptions and also due to degassing from the Earth's crust. Identifying these secular trends in the background stratospheric aerosol system is crucial to predict future aerosol levels [24]. While *Deshler et al.* [13,25] observed no discernable long-term trends in the non-volcanic component of stratospheric aerosols over an extended period (1970-2004), *Hofmann et al.* [26] could observe a significant enhancement in the lower stratospheric aerosol load for the past several years (2000-2008) which they attributed to the increase in anthropogenic sulfur emission. Moreover, eruptions of a few minor volcanoes such as Manam, Ruang, Revantador and Soufriere also might have disturbed the background stratospheric aerosol level to a smaller extent. Although the volcanic degassing during the quiescent and the small eruptive volcanic periods contributes only 14% to total global SO_2 emissions, its efficiency on total atmospheric SO_2 burden is found to be much higher (factor of 5) than that of anthropogenic emissions. Model calculations [27] shows that even though the source strength of volcanic emissions is less than 20 % of the anthropogenic component, the flux of sulfur gases from volcanoes during this period leads to a sulfate burden in the free troposphere which is comparable to that from anthropogenic emissions. This is caused mainly by the altitude-latitude distribution of volcanic emissions, and is most pronounced in tropical latitudes [27].

The quasi-biennial oscillation in stratospheric zonal wind (QBO_U) is found to influence significantly the distribution of volcanic stratospheric aerosols mainly over the tropics [28-30]. Even though, recent observational studies [26,31] revealed significant seasonal and inter-annual variations in the stratospheric aerosol load during the volcanically quiescent period, studies on the influence of these types of periodic oscillations on the stratospheric aerosol distribution over the tropics during volcanically quiescent periods are very rare [11]. This study involves an attempt to study the features of particulates in the UTLS region during the relatively quiescent volcanic period (1998-2005) using global aerosol data from Stratospheric Aerosol and Gas Experiment (SAGE-II) archive and lidar data from Gadanki [13.5°N, 79.2°E]. Formation of semitransparent cirrus (STC) is very common in the upper troposphere. The characteristics of these STCs and their contribution to particulate scattering in UTLS region are also investigated.

2. Extinction/Backscatter data from LIDAR and SAGE-II

The biaxial, monostatic dual polarization Lidar at the National Atmospheric Research Laboratory (NARL), Gadanki, is used to study the scattering properties of atmospheric

particulates in the UTLS region. This Lidar [7] is equipped with Nd:YAG laser (Model: PL8020, Continuum, USA) emitting linearly polarized pulses with 7 ns width and 20 Hz repetition rate at its second harmonic wavelength of 532 nm with a pulse energy of 550 mJ. The basic beam emerging from the laser source with a divergence of 0.45 m rad is expanded using a 10X beam expander to reduce the divergence to <0.1 m rad before transmitting vertically into the atmosphere. The time series of backscattered photons from different altitudes corresponding to each transmitter pulse are received using a 350 mm diameter Schmidt-Cassegrain telescope having a field of view of ~1 m rad. Both the transmitted beam and vertically looking receiving telescope are configured with a fixed horizontal separation of ~3 m. For this lidar configuration, as the lowest altitude at which the full overlap of the transmitter beam with the receiver field-of-view (beam-filled condition) is encountered around 7 km, the data from altitudes above 8 km only are used for retrieving the aerosol properties. A polarized beam splitter in the receiver beam path splits the beam into co-polarized and cross-polarized components which are detected independently using two identical photomultiplier tubes operated in photon counting mode and acquired with a bin width of 2 μs corresponding to an altitude resolution of 300 m. These photon-number profiles corresponding to each transmitted pulse are summed over 250 s to achieve a good signal to noise ratio up to altitude above ~40 km.

The SAGE-II onboard the Earth Radiation Budget Satellite (ERBS) employs solar occultation technique to measure the attenuation of solar radiation at the Earth's limb between the satellite and the Sun due to scattering and absorption by different atmospheric species [32]. These measurements provide the altitude profile of the volume extinction coefficients of atmospheric particulates which includes particles of thin sub-visual cirrus clouds and aerosols at four different wavelengths in the visible and near-IR range (1020, 525, 453 and 385 nm) with a horizontal resolution of about 200 km and a vertical resolution of 0.5 km [33]. This sensor takes 30 occultation observations on a single day, which are equally spaced in longitude round the globe but vary in latitude by a few degrees giving a near global coverage over a period of 25–40 days. Details regarding the SAGE instrumentation and algorithms are discussed in earlier publications [32,34]. The upper limit of the particulate extinction measurable by SAGE sensor at 1020 nm is ~2 x 10^{-2} km^{-1}, which is much larger than that in the UTLS region (~2 x 10^{-4} km^{-1}) under volcanically quiescent period. Cirrus cloud with extinction greater than this value, generally referred to as 'opaque clouds' [35,36], are not measurable by the SAGE-II sensor. Presence of such clouds, limits the SAGE measurements below tropopause.

3. Estimation of particulate extinction from lidar data

The lidar data (backscattered signal) on different nights from Gadanki are used to derive the altitude profiles of particulate backscatter coefficient (β_P) and volume depolarization ratio (δ) [37-39]. In the lidar system, received backscattered signal (at 532 nm wavelength) is separated into co-polarized and cross-polarized components ($\perp$ and $\parallel$ channels, respectively) and recorded separately in two channels. The data in these two channels are analyzed separately employing the Fernald's algorithm [40] to estimate the total

backscattering coefficients ($\beta_\perp$ and $\beta_\parallel$, respectively) taking 30 km as the reference altitude where the aerosol contribution is assumed to be negligible. For this inversion a value of 40 sr^{-1} is assigned for the lidar ratio (S_P) and its variation with altitude depending on δ is also accounted appropriately. With this correction the value of S_P reduces to ~26 sr^{-1} within the STC [39] in the upper troposphere. Further incorporating the correction for multiple scattering the value of S_P within the STC reduces to 20 sr^{-1} (which is used to study the properties of STCs). The molecular backscatter coefficients for the two polarized components are estimated from the mean molecular number density profile taking a molecular depolarization factor (δ_m) of 0.028 [41]. The molecular backscatter coefficient of the co-polarized component ($\beta_{m\perp}$) is related to that of the cross-polarized component ($\beta_{m\parallel}$) as $\beta_{m\perp} = \delta_m \beta_{m\parallel}$. Subtracting $\beta_{m\perp}$ and $\beta_{m\parallel}$ from the altitude profiles of $\beta_\perp$ and $\beta_\parallel$, respectively obtained from lidar data employing the Fernald's algorithm, the altitude profiles of particulate backscatter coefficient, $\beta_{P\perp}$ and $\beta_{P\parallel}$, are estimated. The respective backscatter ratios for the co-polarized ($R_\perp$) and cross-polarized ($R_\parallel$) components are estimated [37] as $R_\perp = \beta_\perp / \beta_{m\perp}$ and $R_\parallel = \beta_\parallel / \beta_{m\parallel}$. As far the net atmospheric backscattering is concerned, the ''unbiased'' or effective backscatter ratio (R) is to be defined , to quantify the gross property of the medium, which on mathematical simplification can be written as $R(h) = [R_\perp(h) + \delta_m R_\parallel(h)]/(1+\delta_m)$. The volume depolarization ratio is obtained from the ratios of $R_\perp$ and $R_\parallel$ as $\delta(h) = [\delta_m R_\parallel(h)]/ R_\perp(h)$. This ratio is a good indicator for distinguishing the cirrus based on 'particle habit'. While for small spherical particles, the values of δ will be relatively small, its value increases significantly as they become large and non- spherical. Using this property of cloud particles, structure and altitude extent of cirrus can be estimated from each lidar profile, which will be used to study the temporal variation of cirrus properties during the entire period of lidar observation. Based on a detailed scrutiny of a number of profiles at different cloud conditions a threshold value of $\delta \geq 0.04$ is assigned for discriminating the STC [42]. If the value of δ exceeds this threshold value it is classified as STC. The effective particulate backscatter coefficient, β_P, is the sum of $\beta_{P\perp}$ and $\beta_{P\parallel}$. The altitude profile of particulate extinction coefficient, α_P, is estimated by multiplying the altitude profile of β_P with the corresponding profile of S_P.

4. Altitude structure of backscatter/extinction, scattering ratio, and depolarization from lidar and comparison with SAGE measurements

Figure 1 shows the altitude profiles of mean particulate backscatter coefficient (β_P), effective backscatter ratio (R) and volume depolarization ratio (δ) for a few nights at Gadanki obtained from Lidar data during the year 1999 as typical samples. In general, β_P and R show a general decrease with increase in altitude (eg. 05 and 12 April 1999) in the troposphere and stratosphere. But on a few nights a significant enhancement is observable over a small region between 9 and 17 km. This sharp increase in β_P is due to strong scattering from ice particles of thin STC layers, formed at these altitudes either by *in situ* condensation of water vapour or originated from the outflow of convective anvils [43-45]. On a few occasions this layer of enhanced β_P extends down, up to 5–6 km, depicting typical case of dense cirrus (9 June 1999), occurring predominantly during the monsoon period. Note that, these STCs are

so transparent that the lidar beam could penetrate the cloud and provide measurable signal even from higher altitudes. The opacity of STCs are quantified using the cloud optical depth (τ_c) which is the height integrated particulate extinction coefficient (α_p), obtained by multiplying β_p with the S_p, from the cloud base (h_{cb}) up to the cloud top (h_{ct}). In case if the cirrus is too dense (with τ_c exceeding 1.5) the lidar beam will not be able to penetrate the cirrus layer impeding useful lidar observations. In association with the enhancement in β_p and R, a significant increase in δ also can be observed at these altitudes. This suggests that the scattering particles within the STCs are relatively large and significantly non-spherical in nature. Depending on τ_c, STCs are further classified [46] in three classes viz., sub-visual cirrus (SVC) with τ_c<0.03, thin cirrus (TC) with 0.03 < τ_c <0.3 and dense cirrus (DC) with τ_c >0.3. General features of STCs from this tropical station [37] showed that while the occurrence of SVC is larger during winter, TC and DC occur more frequently during the monsoon period. The upper and lower boundaries of STCs are identified from altitude profiles of R and δ using a threshold condition [37,42] for R to exceed 2 in either of the two lidar channels ($\perp$ or $\parallel$ channels) along with the value of δ exceeding 0.04 in the altitude region where the STCs are usually observed (8 to 20 km).

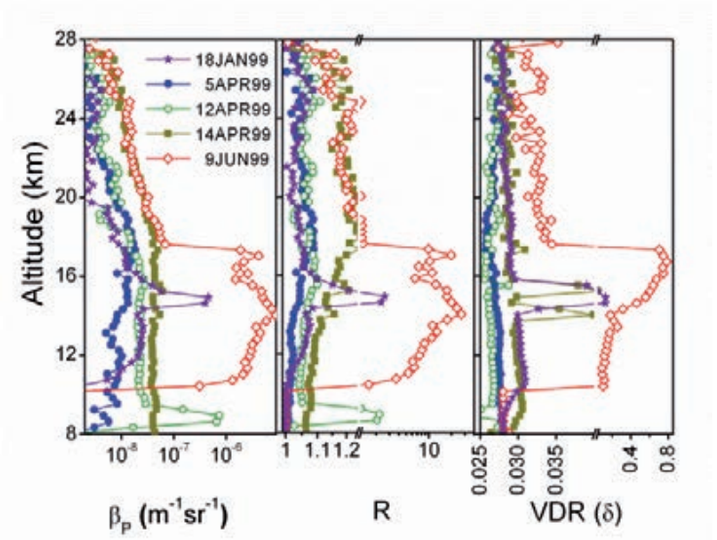

Figure 1. Altitude profiles of mean particulate backscatter coefficient (β_p), effective backscatter ratio (R) and volume depolarization ratio (δ) for few nights during the year 1999

A detailed error analysis [42] showed that the estimated values of β_p is less sensitive to the variability in S_p. For a given uncertainty of 25% in S_p, the maximum uncertainty in β_p is 10% in the absence of clouds, ~15% for thin cirrus and ~30% for thick cirrus. For the same uncertainty in S_p, the maximum uncertainty in the retrieved backscatter coefficient and effective backscatter ratio are around 0.6%, 2% and 10%, respectively, for clear atmosphere, atmosphere with thin cirrus and atmosphere with thick cirrus. Including the possible errors in the lidar signal inversion associated with the uncertainty in the molecular backscatter coefficient, the resultant error in the derived optical depth would be ~20%. As the signal-to-noise ratio is >2 up to ~45 km, for altitudes <30 km the system induced errors will be significantly small (<1%) compared to that from other sources. The error due to the influence

of background and system noise is negligible (< 0.001%) compared to that due to the uncertainty in S_P.

Altitude profiles of α_P at 525 and 1020 nm from Global SAGE-II aerosol data archive (version 6.2) during the period 1998-2005 are obtained through the NASA website *http://wwwsage2.larc.nasa.gov/data/v6_data*. Typical estimated error in SAGE-II measured α_P at 525 and 1020 nm are in the range 10 to 15% [34]. Figure 2 show a comparison of α_P obtained from the SAGE-II at 525 and 1020 nm along with that of the lidar at 532 nm in the altitude region 10–30 km for a few sunset occultation events during the period 1998–2003. These comparisons are made when SAGE-II had an occultation pass within a grid size of ± 5° in latitude and ±10° in longitude centered at Gadanki within a time-duration of 1 day with respect to the lidar observation. As the difference between the SAGE-II wavelength of 525 nm and lidar wavelength of 532 nm is less than 1.5%, the expected absolute differences in α_P for these two wavelengths would be almost insignificant [47]. The latitude and longitude of line-of-sight tangent point of SAGE-II for each occultation event are shown in the respective frames of Figure 2. The radial distance, d, between the tangent point and the lidar location estimated from the latitudinal and longitudinal differences between the two is also marked in this figure. In general, the shape of the SAGE-II and lidar-derived extinction profiles show a good agreement especially in the stratosphere. The mean percentage difference for

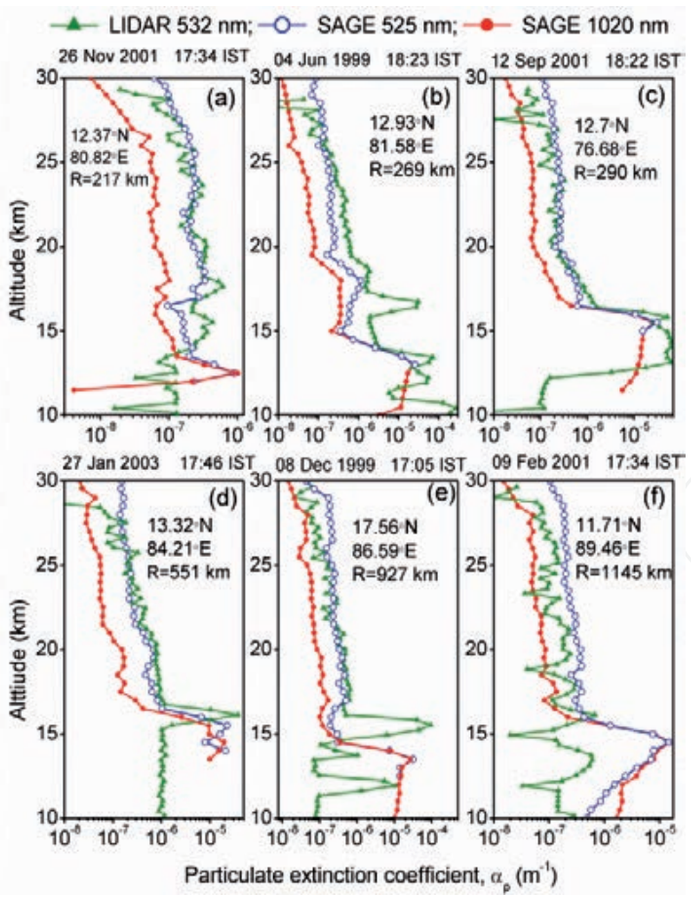

Figure 2. A comparison of the altitude profiles of α_P on a few days derived from lidar data (532nm) at Gadanki, along with that of SAGE-II (525 and 1020 nm) sunset occultation events near this region.

extinction measured by the two instruments in the altitude range 18–25 km is <40%, which is comparable in magnitude with those obtained in other similar inter-comparisons [48-50]. For Altitudes <17 and >25 km, both mean differences and standard deviations are relatively large (< 40%). This could partly be due to the temporal variations during the course of the two measurements as well as the spatial heterogeneity (between the locations of the two measurements). The observed increase in deviation below 17 km is partly due to the influence of STCs in the UT region as well as their spatial heterogeneity.

5. Semitransparent cirrus in the upper troposphere

Space-borne lidars, *in situ* measurements and ground-based experiments indicates frequent manifestation of cirrus clouds in the upper troposphere [36,51-53]. The frequency of occurrence of STC (F_{STC}) over a wide geographical region can be derived from VHRR data from remote sensing satellites. The geostationary meteorological satellite, KALPANA-1, positioned at 74°E over the equator for continuous measurements of clouds and convective systems, provides the required information over the Indian region. This satellite observes the earth in three wavelength bands: Visible (0.55–0.75 μm), Water vapor band (WV: 5.7–7.1 μm), and the atmospheric window of thermal infrared (TIR: 10.5–12.5 μm).. In TIR and WV bands, the data is recorded at a pixel resolution of 8 km (nadir) with a digital resolution of 10 bits. Unless the cloud is optically thick, the radiance observed in TIR band does not correspond only to the cloud top, but is also weighted by the radiation emitted from the altitudes below. The brightness temperatures measured in these two channels are used to detect STC following the bi-spectral approach of Roca et al. [54]. In this method all the cloudy pixels having WV brightness temperature < 246 K and TIR brightness temperature > 270 K are treated as STC. In addition to the above, those cloudy pixels having a brightness temperature difference > 20 K between the two channels and having WV brightness temperature < 246 K, a condition imposed mainly to detect STC above other low level clouds, also are treated as STC [55]. Figure 3 shows the frequency of occurrence of STC (F_{STC}) over the Indian region in different months for the year 2005 derived from KALPANA-1 data. Any thin cirrus cloud above a deep convective cloud cannot be detected by the present bi-spectral algorithm, unless the difference in brightness temperature in the two channels exceeds 20 K (indicating significant altitudinal separation between the top of the STC and the optically dense high-altitude cloud), which may not be the case if STC forms just above the high altitude cloud. Because of this inherent limitation, the estimated F_{STC} will always be an underestimate over the region where high-altitude clouds are present. Hence the regions where the monthly mean frequency of occurrence of high-altitude clouds larger than 20% are masked (dark brown) in Figure 3.

For studying the role of deep convection on the genesis of STC, the monthly mean spatial distribution of the frequency of occurrence of deep clouds (F_D) with TIR brightness temperature < 235 K derived from KALPANA-1 during January-December 2005 are presented in Figure 4. A comparison of Figures 3 and 4 suggests that that the longitudinally extended band of high F_{STC} (~40-60%) in the region 10°S-20°S over the western tropical Indian Ocean and around the equator over the eastern Indian Ocean in January (Figure 3) is

closely associated with the deep convection linked to the Inter tropical convergence Zone. However, the values of F_{STC} far exceed F_D over all these regions. During this month, the highest values of F_{STC} (~60%) are observed at the north of Madagascar in the western Indian Ocean and over Sumatra/Indonesia in the eastern Indian Ocean, where the frequency of occurrence of very large deep convection is quite large. A region of less cloudiness (with F_{STC}<15%) is observed in the central Arabian Sea and Indian Peninsula centered around 5°N-15°N, which runs parallel to the equatorial band of high STC occurrence and is well separated from the deep convective regions. A similar STC-free zone is also observed in the southeast Indian Ocean centered on 20°S. Clearly, these regions with low occurrence of STC are caused by the large subsidence in the upper troposphere associated with the descending limb of the Hadley circulation cell.

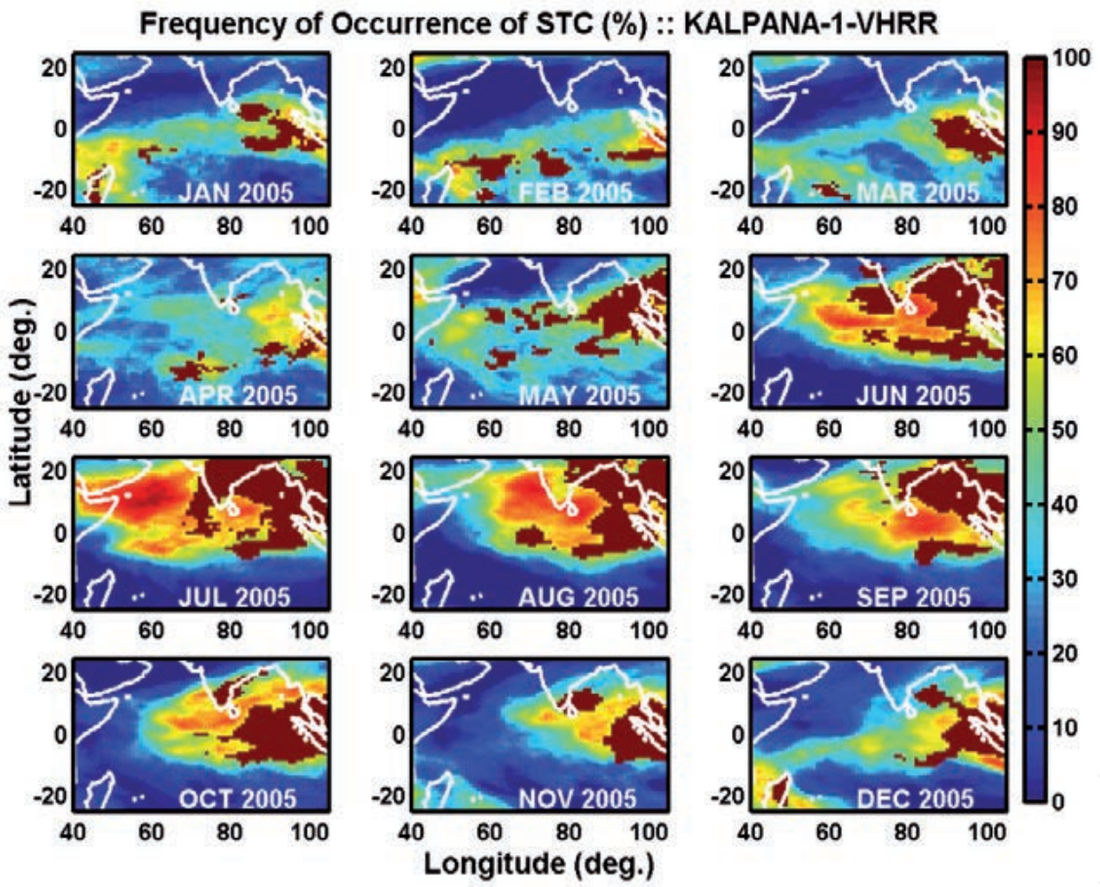

Figure 3. Spatial variation of mean STC occurrence in different months during the year 2005 (brown color shows the region where the STC retrieval was not possible due to the presence of high clouds) derived from the KALPANA-1 VHRR data

6. General features of STC over the Indian region

Lidar studies from Gadanki indicate that the occurrence of STC in this geographical region is the largest from May-October, associated with the formation of intense convection and the subsequent onset of Asian summer monsoon (ASM). Figure 5 shows the mean feature of STC occurrence and its altitude extend averaged for the period 1998-2003. While the STCs

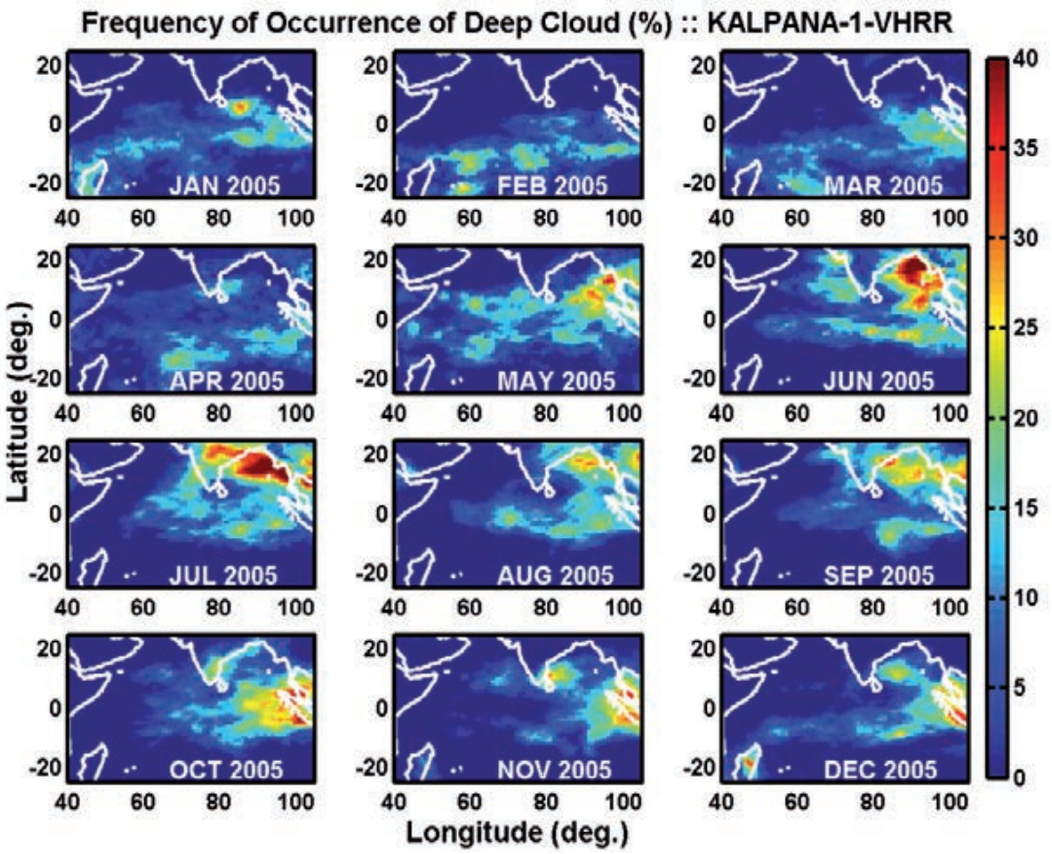

Figure 4. Spatial variation of deep convective clouds in different months during the year 2005 derived from the KALPANA-1VHRR data

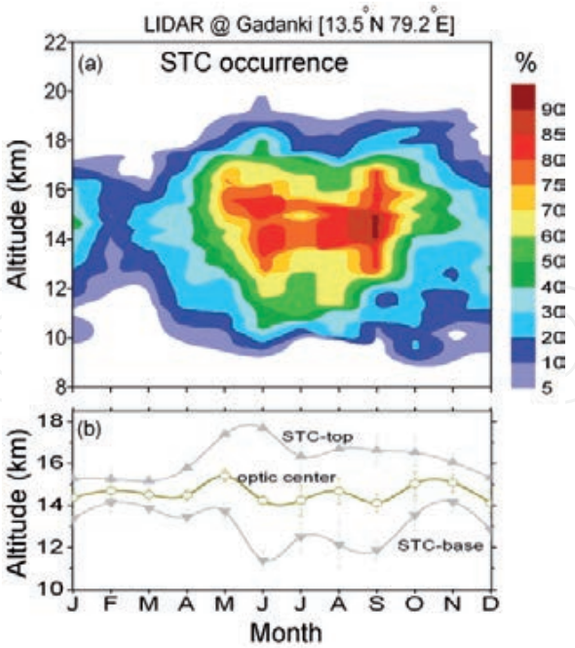

Figure 5. Month-to-month variation of the normalized frequency of encountering STC at different attitudes in the upper troposphere (a) along with the month-to-month variation of the mean top, base and optic center of STC with vertical bars indicating the standard error (b) from lidar data at Gadanki for the period 1998–2003.

occurring during the period May- October are generally thick and optically denser [37], those occurring during the rest of the year (dry months) are relatively thin (both geometrically and optically). As the Gadanki region is almost free from deep convection (Figure 4) during winter, the STCs forming during this period could be of *in situ* origin. While the dense STCs observed during the May-October period are associated with deep convection over the Indian land mass and Bay of Bengal.

On examining the frequency of occurrence of STC during the period 1998-2003 (Figure 6a) it can be seen that the frequency of occurrence of SVC is much larger than TC and DC. In general, STCs are observed in the altitude region 10 to 18 km with a preferred altitude (frequent occurrence) region between 14 and 16 km (Figure 6b) Thin clouds occur more frequently than thick clouds (Figure 6c). Though the vertical extent of STC generally vary from 0.4 to ~ 4.0 km in majority of the cases it is less than 1.7 km. Though the volume depolarization,δ, in these clouds varies in the range 0.03 to 0.6 its distribution peaks (Figure 6d) in the lowest value. The value of δ for SVC and TC are generally very small compared to DC. The particulate depolarization (δ_p) of STC (Figure 6e) generally varies from zero to unity. The distribution of δp peaks around a value of 0.15. The properties of STC vary significantly with cloud temperature (or altitude). Figure 7 shows the variation of thickness, depolarization and optical depth of STC with cloud temperature. As can be seen from Figure 7a, the thickness of STC is a maximum for temperatures in the range –55° to –75°C. Above and below this temperature range the cloud thickness decreases. Similarly the depolarization is maximum around –75°C and decreases steadily with increase in

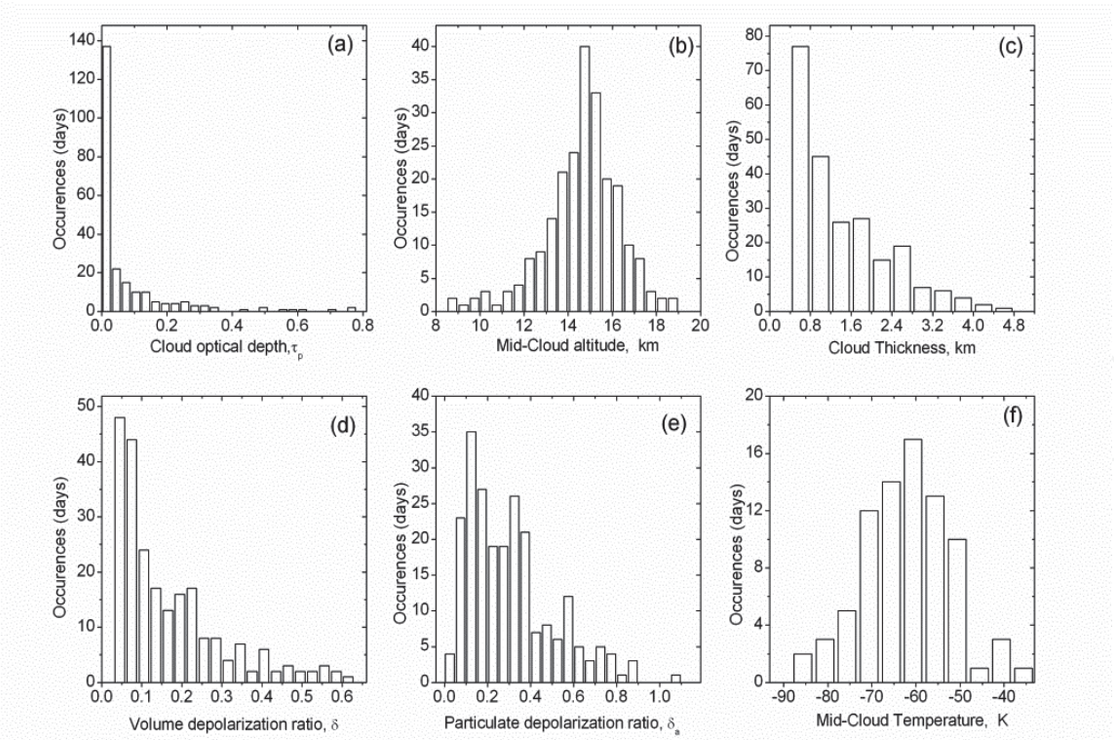

Figure 6. Frequency distribution of (a) cloud optical depth, (b) mid-cloud altitude (optic center), (c) Geometrical thickness, (e) Volume Depolarization Ratio, (f) Particulate depolarization, and (g) Mid-cloud temperature of STCs observed at Gadanki for the period 1998-2003.

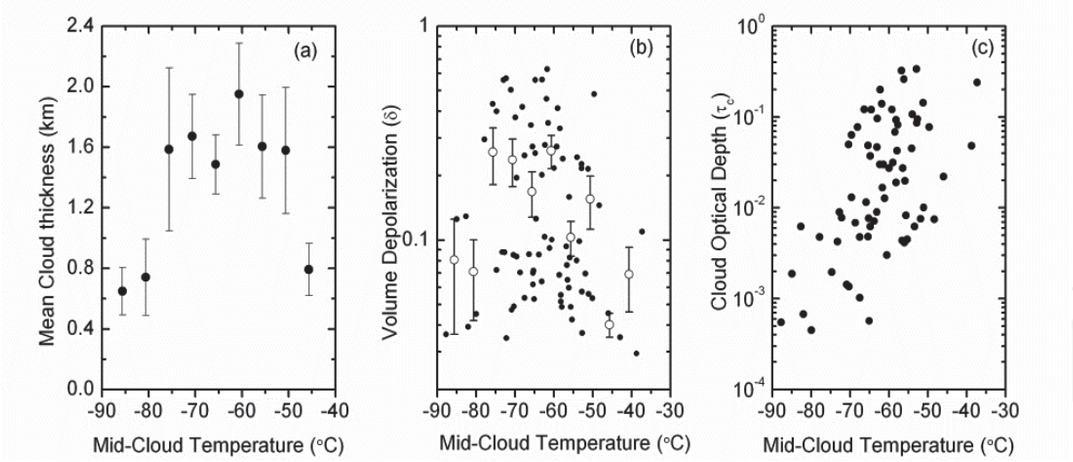

Figure 7. Mean variation of Cloud thickness, Volume Depolarization Ratio and cloud optical depth with mid-cloud temperature for STCs observed at Gadanki during the period 1998-2003.

temperature. The value of δ also shows a sharp decrease when the cloud temperature decreases below –75°C. The decrease in δ with increase in temperature can be attributed to the melting and evaporation of ice crystals and subsequent blunting of their edges [56]. Decrease in temperature leads formation of particles with sharp edges. But when the temperature decreases below a threshold value, the particle size [56] becomes small (needle type). This can lead to a decrease in δ. Figure 7c shows that on an average τ_c increases with increase in temperature. The cloud becomes more opaque at higher temperatures. This has important implication in the radiative effects of STCs [38] in the context of global change.

7. Mean annual variation of particulate scattering in the UTLS region

Figure 8a shows a contour plot of the logarithm of mean β_p as a function of month and altitude for the period 1998–2003. The values of β_p are relatively large during the May to September period and small during the winter months. This is due to the influence of STC. Relatively high values of β_p in the UT region during the monsoon period are due to the presence of relatively dense cirrus and low values during winter are due to the presence of SVC. In contrast to the UT region, β_p in the LS is generally large (as high as 6×10^{-8} m^{-1} sr^{-1}) during the winter (November to January) and pre-monsoon (April–May) months and low (as low as 10^{-9} m^{-1} sr^{-1}) during the summer (July and August) months. Prominent peaks are observed during May–June and November–January periods with low values in July–August and February. The mean annual pattern of α_p at different altitudes from the lidar derived β_p (Figure8a) is presented in Figure 8b. Similar grading scheme is used in both these plots to make an easy direct visual comparison of the pattern. The major features of the annual variation of β_p and α_p in different altitudes are very similar in these two plots, even though the lidar ratio is assumed to be variable with altitude depending on aerosol properties.

Microphysical properties like the size and shape of particles in the UTLS region can be delineated from the depolarization of backscattered radiation [57,58]. Figure 8c shows a contour plot of monthly mean δ in the altitude region 8–28 km. The value of δ varies in the range 0.03 to 0.6 in UT region and from 0.03– 0.04 in the LS region. High values of δ are

generally confined to a narrow altitude region (14–16 km) during winter while these extend to a wider altitude region (12– 18 km) during summer monsoon period. High values of δ (>0.2) are observed in the altitude region 14– 16 km during April–October period. Values of δ exceeding 0.04 observed in the UT (above 10 km) are mainly due to presence of highly non-spherical ice particles associated with STC [37]. The overall low values of δ suggests that particles in the LS region are very small and tend to become more spherical in nature.

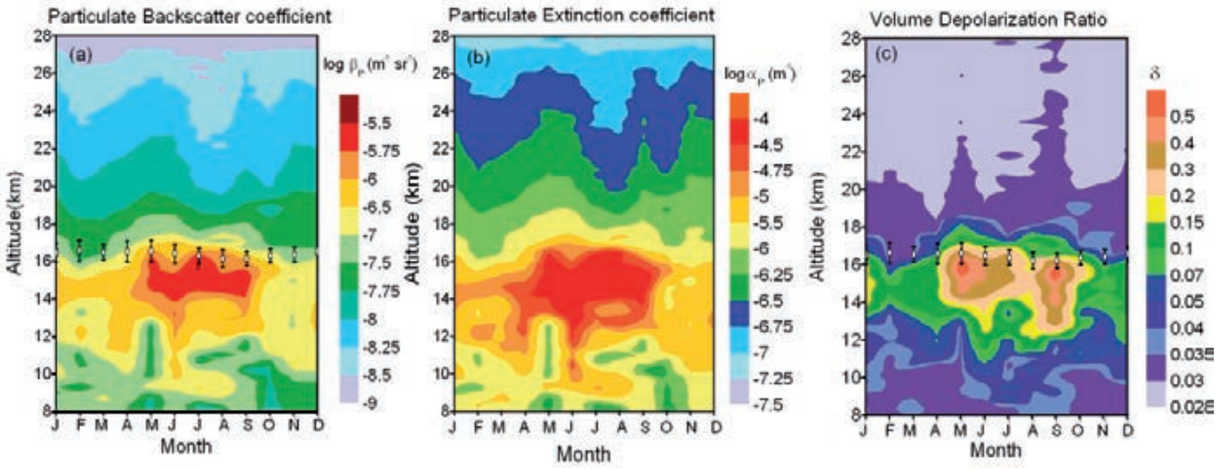

Figure 8. Contour plot of mean particulate backscatter coefficient (βp) and extinction coefficient (αp) in logarithmic scale along with the volume depolarization ratio (δ) as a function of month and altitude for the period 1998–2003 derived from lidar data. Mean cold point tropopause altitude is superposed over the contour along with its standard deviation.

Figure 9 shows a contour plot of α_p similar to Figure 8b but generated from SAGE-II derived mean particulate extinction at 525 nm and 1020 nm over a small geographical grid size of 10-16°N and 73-86°E centered around Gadanki. As thin STCs in the UT region significantly attenuates the SAGE-II wavelengths, (especially that at 525 nm) there will be a large data gap at the lower altitudes. The region bound between X-axis and the rectangular vertical bars (shown white) are the data gaps. As the attenuation for 1020 nm is less than that for 525 nm this wavelength can penetrate to lower altitudes to yield useful data. The data gap is relatively less for 1020 nm. However, in generating the contours, the data gap is appropriately interpolated. General similarity of the pattern in Figure 9a and 9b suggests that the interpolation did not influence the major features of Figure 9b. Except for an overall decrease in the values of α_p derived from SAGE-II (at 525nm) compared to those derived from lidar data, the major spatio-temporal features in Figure 9 also matches well with those of Figure 8b. Thus, the inferences derived from lidar data is reconfirmed by SAGE-II observations during the same period.

To make the features more concise, the month to month variation of altitude weighted δ (altitude integral of δ normalized to the slab thickness) for different altitude regions with a slab thickness of 2 km are examined in the UT and LS region. Though a sharp definition of UT and LS region is rather difficult, for the present analysis we use the term UT for the altitude region from 10 to 16 km and LS from 18 to ~30 km. Though the cold point tropopause shows a small variation with time of the day and day of the year, it lies always

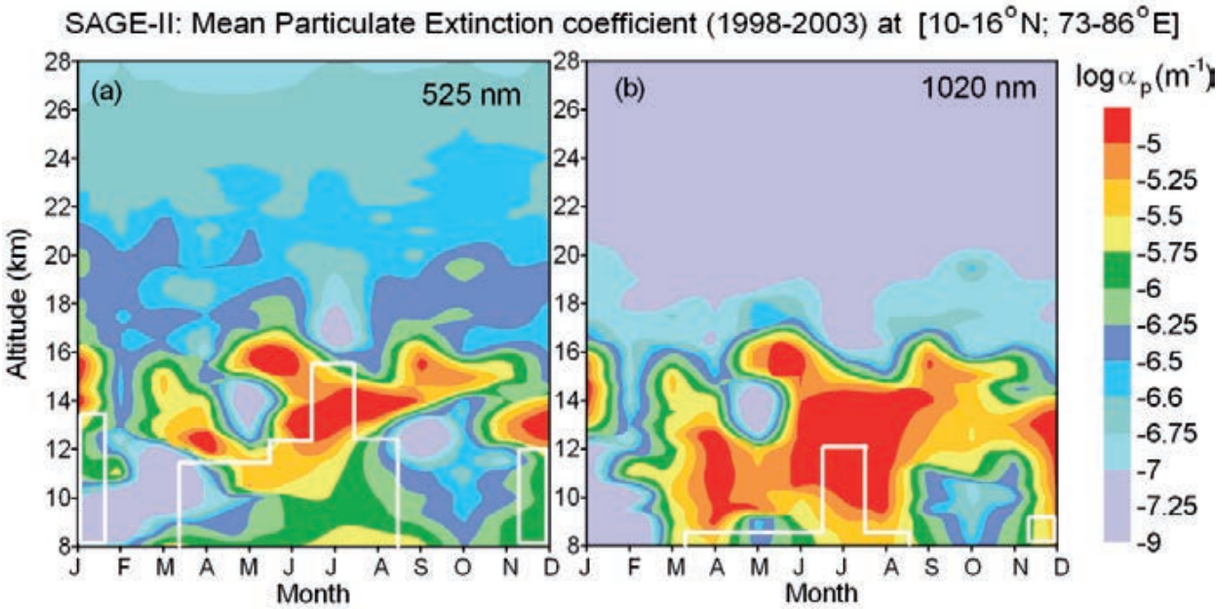

Figure 9. Contour plots of mean particulate extinction coefficient (α_P), in logarithmic scale, at 525nm and 1020 nm as a function of month and altitude for the period 1998–2003 from SAGE-II observations

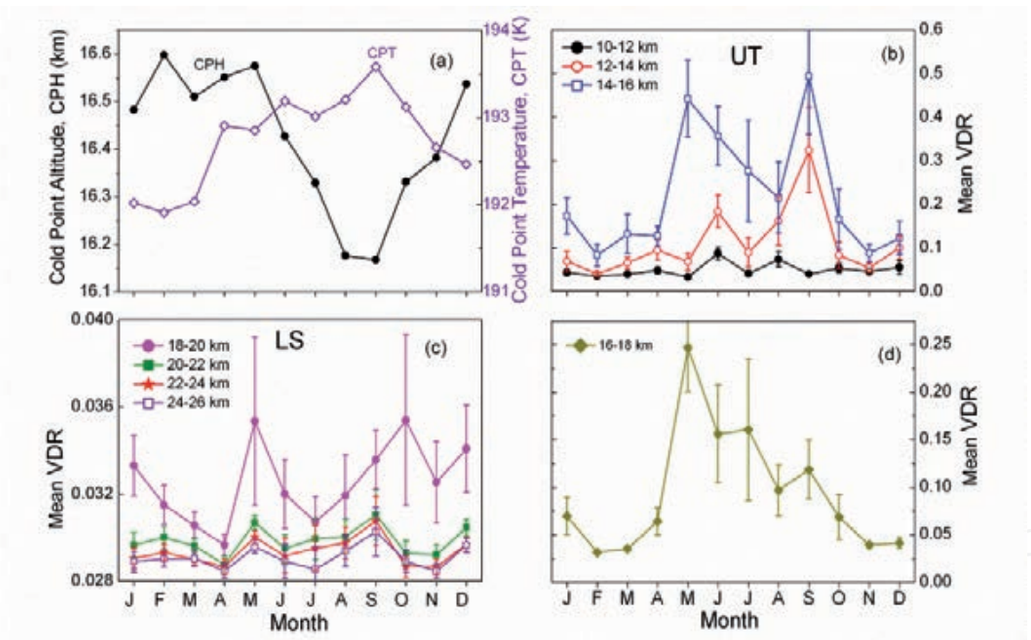

Figure 10. (a) Mean annual variation of cold point tropopause temperature and altitude along with the mean annual variation of integrated volume depolarization ratio (VDR) normalized to the slab thickness of 2 km at different altitudes (b) in the upper troposphere, (c) in the lower stratosphere and (d) in the tropopause region.

in the range 16–18 km (a transition region), such that the region defined as UT is always below cold point and region defined as LS is above. Figure 10a shows the mean annual variation of the cold point tropopause altitude and tropopause temperature.

The annual variation of δ for different altitudes in UT is shown in Figure 10b and that in LS in Figure 10c. Though, in general, on an average, the value of δ in LS region is < 0.04, it

shows a pronounced oscillation with prominent peaks in May and September–January period. Above 20 km, the value of mean δ (~0.03) is very close to the molecular depolarization, it is relatively large (in the range 0.03 – 0.04) in the altitude region 18–20 km just above the cold point tropical tropopause. Thus, in the LS region, the particle size and non-sphericity decreases with increase in altitude. Note that, the value of δ encountered in this region is less than the threshold value (0.04) used for identifying the cirrus particles. The value of δ is largest in the altitude region 14–16 km, just below the mean level of tropical tropopause. The general similarity in the annual variation of δ in the altitude regions 14–16 km and 10-12 km indicates that the particle microphysics in these altitudes are strongly coupled. Even though the cold point tropopause altitude shows a small variation from month-to-month, the mean level lies around 16.5 km. Figure 10d shows the mean annual variation of the altitude weighted δ around the cold point tropopause for a slab thickness of 2 km. The observed general similarity of the annual variation of δ in the entire region from 10 to 20 km indicates that the annual variation of the particle habit (size and shape) in the UT and LS regions are strongly coupled. The observed general decrease in δ from UT to LS suggests that the particles tend to become small and more regular in shape with increase in altitude.

8. Effect of tropospheric convection on UTLS particulates

During the ASM period, the upper troposphere is significantly influenced by the tropospheric convection. This in turn could influence the microphysical properties of UTLS particulates. The outgoing long wave radiation (OLR), which is directly influenced by cloud cover and in turn by convection, could be effectively used as a proxy to the strength of tropospheric convection [59] and the seasonal variation of deep convection. The value of mean OLR is generally high for clear sky condition (~460 W m^{-2}) and decreases with increase in cloud cover and cloud vertical extent. A threshold value [60] of 200 Wm^{-2} for OLR which when declines below could be treated as in index for deep convection. The percentage of occurrence of daily mean OLR with its value < 200 Wm^{-2}, within a grid size of 2.5° × 2.5° over a geographical region 12.5° –15° N in latitude and 77.5° –80° E in longitude obtained from NCEP/NCAR reanalysis provided by the Climate Diagnostic Center through their Web site at http://www.cdc.noaa.gov/ averaged in different months for the period 1998–2003, which is almost negligible during the December to April period, starts increasing from May and shows a broad peak during the period June to October (Figure 11a).

The strength of tropospheric convection also can be assessed from the convective available potential energy (CAPE), defined as the altitude integrated buoyancy of lifted air parcel from the level of free convection to the level of neutral buoyancy [61], is estimated from the altitude profile of potential temperature as $CAPE = \int [g(q_v - q_T)/q_T]dz$, where q_v is the virtual potential temperature of the air parcel, q_T is the environmental potential temperature and g is acceleration due to gravity. The integral is taken from the level of free convection to the level of neutral buoyancy. The mean values of CAPE, which is a measure of stability in the atmosphere as far as vertical displacements are concerned [62], in different months for Chennai (13°N, 80.2°E), a station located very close to Gadanki, obtained through India

Meteorology Department (Web site http://www.weather.uwyo.edu/upperair/sounding.html.) are presented in Figure 11b. The CAPE also shows a prominent peak during the period April to May along with a small secondary peak in September. Intense convection is closely related to thunderstorm activity. Climatologically averaged thunderstorm activity in different latitude belts over the Indian subcontinent was investigated in detail in earlier study [63]. The annual variation of the mean number of thunderstorm days for the latitude belt 10–15°N (Figure 11c) shows two prominent peaks in May and September–October period. Deep convection and high thunderstorm activity leads to the formation of thick convective clouds. The main reason for low lidar observation statistics during the monsoon period is the presence of these convective clouds which impede the observations. Though these clouds will have a large spatial extent and persist for several days, some gap region which is devoid of thick clouds (favouring lidar observation) starts developing after a few days The outflow from adjacent convective anvils spreading over to this gap region leads to the formation of STCs.

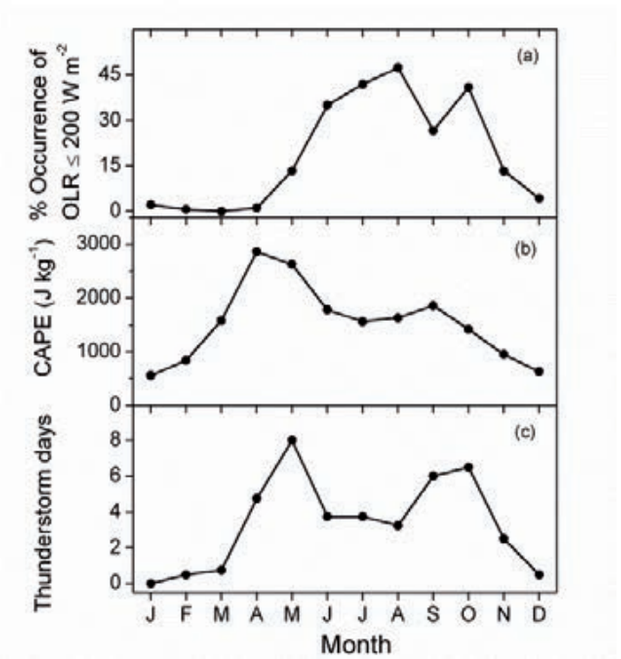

Figure 11. Annual variation of the (a) frequency distribution of outgoing long-wave radiation (<200 Wm^{-2}) around Gadanki between 12.5°–15°N and 77.5°–80°E along with (b) convective available potential energy (CAPE) obtained from Radiosonde observations at Chennai during the period 1998–2003. (c) Month-to-month variation of mean number of thunderstorm days (TSD) for the latitude belt 10–15°N during the period 1970–1980 [63].

Being originated from convective outflow [43,44], especially during the summer monsoon period, particles of STCs in the UT region during this period will be relatively large and highly non-spherical [8,45]. Presence of these large non-spherical particles leads to an increase of δ in this region, as is observed. Subsequent uplift of some of these particles along with tropospheric air across the tropopause leads to an increase in δ along with the integrated backscatter ($I\beta_P$) in the region just above the cold point tropopause. As the particles and precursor gases are not directly injected into the stratosphere but diffuse

slowly across the tropopause they confine to a small region just above the cold point tropopause. Note that during the period July to August when CAPE as well as thunderstorm activity shows a small decrease, δ (Figure 12) and $I\beta_P$ (Figure 13) in the 18–20 km also shows a decrease. However, the STCs during this period shows large spatio-temporal variations [37] introducing large day-to-day variability in $I\beta_P$ and δ in the UT and LS region as indicated by the large error bars during the May-October period.

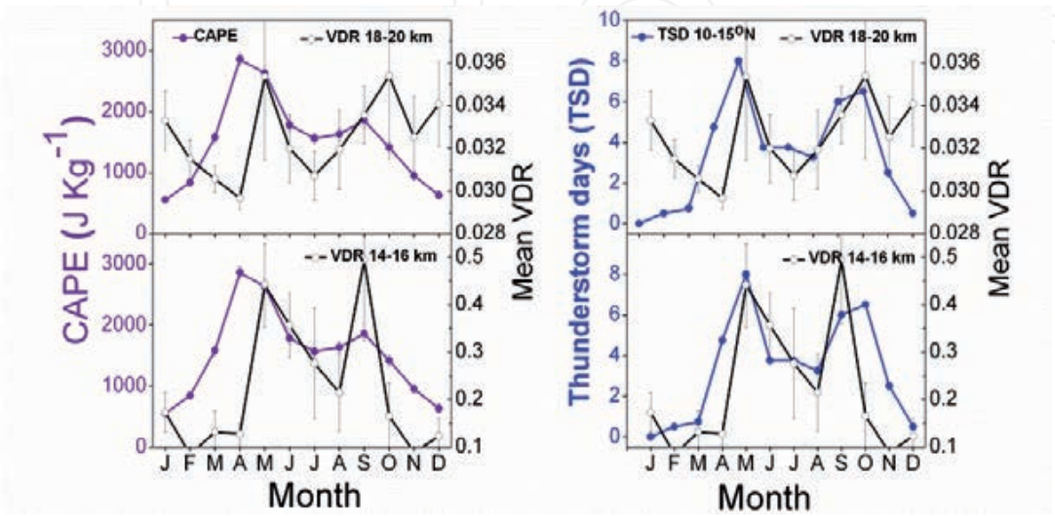

Figure 12. Mean annual variation of integrated volume depolarization ratio (VDR) normalized to the slab thickness of 2 km in the altitude region 14-16 km (UT) and 18-20 km (LS) superposed on the annual variation of CAPE and number of thunderstorm days. Vertical bars represent the respective standard error.

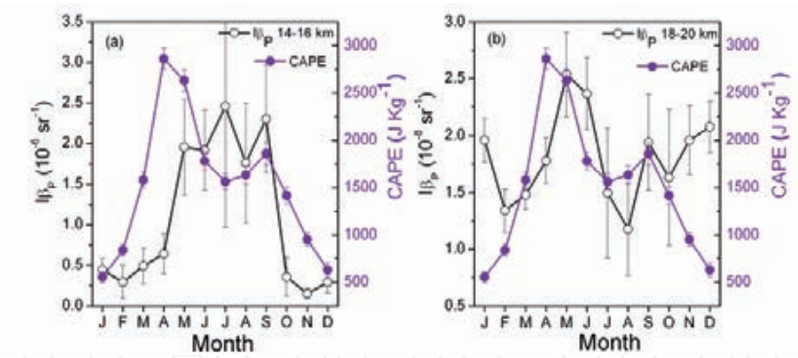

Figure 13. Mean annual variation of Integrated Particulate Back scatter ($I\beta_P$) in UT (a) and LS (b) superimposed on the annual variation of CAPE for the period 1998-2003.Vertical bars represent the standard error.

Though during the December–February period CAPE is relatively small and thunderstorm activity also is less, a broad peak in $I\beta_P$ at 18–20 km is observable during this period (Figure 13).This feature though appears to be contradicting to the above hypothesis proposed for the summer monsoon period, the real mechanism responsible for the transport of tropospheric air into the stratosphere during winter is different from that during the monsoon period. During winter the intrusion of tropospheric air into the lower stratosphere occurs through vertical ascent of air driven by the strength of the ascending branch of the Hadley cell

circulation in the troposphere and Brewer- Dobson circulation (B–D) in the UTLS region. The B–D circulation is primarily driven by mechanical forcing (westward directed wave drag) arising from the dissipation of planetary-scale waves (breaking of Rossby waves) in the extra tropical stratosphere [64]. Because of filtering by the large-scale stratospheric winds, vertical propagation of planetary waves into the extra-tropical stratosphere occurs primarily during winter and this seasonality in wave forcing accounts for the winter maximum in the B–D circulation [65,66]. In association with these processes, the cold point tropopause at tropics is pushed to a higher altitude during winter and they play a major role in exchange of mass from troposphere to stratosphere.

As can be seen from Figure 10a the tropopause is cooler and higher during the January–March period and warmer and lower during August–October period which is in accordance with what is reported for tropical locations [67-70]. These Seasonal changes in the cold point tropopause altitude also contribute to the mass influx to stratosphere [71-73]. Transport of constituents like water vapor, aerosols, trace gases etc across the tropopause which acts as a permeable membrane through which continuous mixing between tropospheric and stratospheric air takes place is well demonstrated by various investigators [74-77]. Over and above the penetration of deep convection, this annual adjustment of tropopause altitude is an important mechanism for the stratosphere troposphere exchange.

9. Contribution of STC to particulate scattering in the UTLS region

Fine ice crystals of STCs originating either through the outflow from deep convective anvils or through freeze drying of moist air lifted up to the tropopause by normal convection contribute significantly for scattering in the UTLS region. In addition, other aerosol particles originating from the surface (mainly through bulk to particle conversion and those of vegetative origin) as well as those formed in the upper troposphere through gas- to-particle conversion (mainly of various industrial gases) also contribute for the particulate loading in the UTLS region. It would be worth examining the relative contributions of the two components in the UTLS region to make a quantitative assessment of the contribution of STCs to the scattering properties in the UTLS region. Figure 8a shows the contour plots of month-to-month variation of mean β_p derived from lidar data during the period 1998–2003 (including both STC-contaminated and STC-free). Note that, as this study period was mostly devoid of major volcanic eruptions [24] the stratospheric aerosol loading can be considered to be in its background level.

While β_p in the UT is a maximum during the May –September period and minimum during October–November, in the lower stratosphere it is minimum during summer (July and August) and maximum during winter. However, the winter high in the LS region was attributed [7] to the transport of tropospheric air (containing aerosols and precursor gases) in conjunction with the tropical upwelling and B– D circulation while the observed high during May–June is due to the upward influx of particles (including ice crystals of STCs) from the UT region. As the uncertainty associated with lidar-derived β_p is small compared to α_p [42], for the lidar based study the altitude profile of β_p and $I\beta_P$ for a desired altitude

region (layer integrated) is used for studying the annual pattern of particulate scattering in the UTLS region. Figure 14 shows the contour plots depicting the annual variation of β_P at different altitudes for the STC-contaminated case and the STC-free case separately.

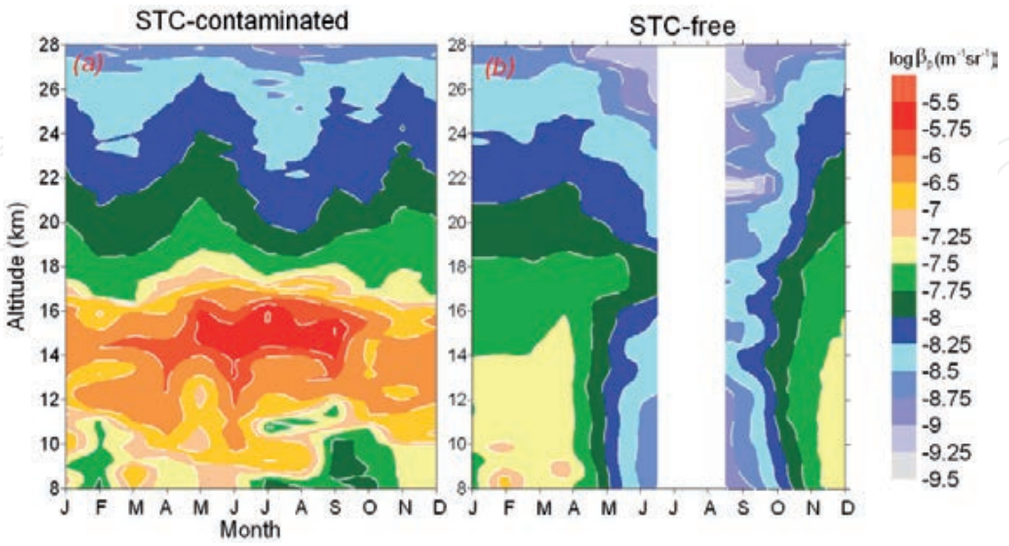

Figure 14. Mean annual variation of particulate backscatter coefficient (β_P) from lidar data at Gadanki for the STC-contaminated (a) and STC-free (b) cases during the period 1998–2003.

The cloud cover being quite large during the summer monsoon period no lidar data were available without STC during the July and August months, which lead to a data-gap for the STC-free case presented in Figure 14b. As can be seen, the variations of β_P in Figure 14a is very similar to those in Figure 8a generated by considering both the STC-contaminated and STC-free profiles even though the absolute magnitude in the UT region is slightly small in the latter case especially during the October–November period. High values of β_P are observed in the UT region for the STC-contaminated case during summer monsoon period. Figure 14b shows that, β_P in the UT region is very small for the STC-free case compared to that of STC-contaminated case for the same period. The values of β_P in the UT region are high during winter and spring and low during summer and autumn for the STC-free case. This annual pattern of β_P is significantly different from that of STC-contaminated case. From this, it is quite reasonable to infer that the prominent peak of β_P in the UT region observed during the summer monsoon period (in Figures 8a and 14a) is due to the influence of STC. However, the enhancement in β_P in the UT region due to STC-contamination is relatively small during the winter months

As seen from Figure 5 the occurrence of STC is mostly confined to the uppermost part of the troposphere, above ~10 km. Because of their presence these STCs directly contribute to the particulate scattering in this region. Over and above, these prevailing STCs in the upper troposphere can also modify the scattering property of particulates (aerosols) above the cloud-top as well as below the cloud-base. These effects in the UT and LS regions can be inferred by examining the $I\beta_P$ at four different altitude regions, 8–10 km (UT_1), 12–16 km (UT_2), 18–21 km (LS_1) and 21–25 km (LS_2). Among these, the LS_1 and LS_2 regions are above

the STC-top while UT_1 is below the STC-base. The month-to-month variation of mean $I\beta_P$ for the three cases; viz, (i) including all profiles (ii) considering only STC-contaminated profiles and (iii) Considering only STC-free profiles, are presented in Figure 15. In the absence of STC the $I\beta_P$ in the UT_2 region is significantly small. The STC contribution to $I\beta_P$ in this region works out to be around 93±5%. The $I\beta_P$ shows an annual variation with relatively high values during the winter/dry months and low during the summer monsoon period for the STC-free case. When STCs prevail, the $I\beta_P$ in the UT_2 region increases significantly especially during the summer monsoon period. Even though the enhancement in $I\beta_P$ due to the presence of STC is seen during the winter/dry months also, its magnitude is relatively less. It would be worth in this context to note that, during the monsoon period, the UT_2 region is dominantly influenced by dense STCs originating from the outflow of convective anvils [78]. The particle associated with these STCs will be relatively large and highly non-spherical [8,45] and hence their contribution to β_P and δ will be significantly large [7].

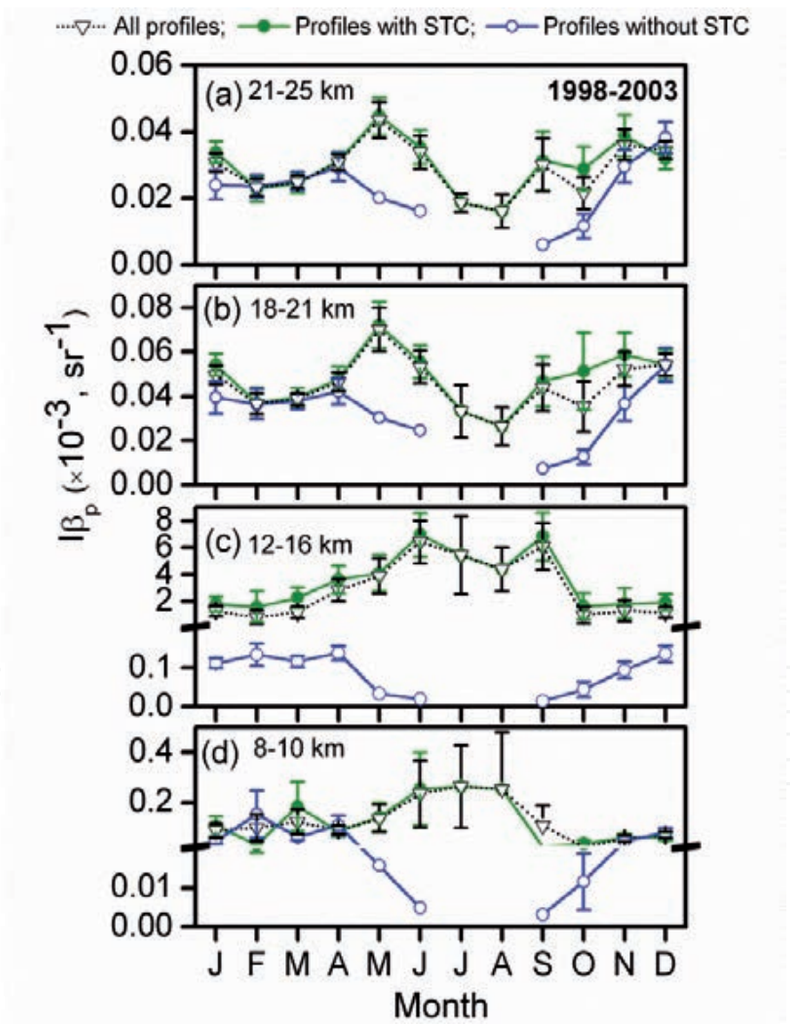

Figure 15. Mean annual variation of layer integrated particulate backscatter coefficient ($I\beta_P$) in LS_2 region (a), LS_1 region (b), UT_2 region (c) and UT_1 region (d), for the three cases (including all profiles, only STC-contaminated profiles and only STC-free profiles) from lidar data at Gadanki, for the period 1998–2003.

It is quite interesting to note that the presence of STC in the UT_2 region significantly enhances the $I\beta_P$ in the lower stratosphere also especially during the May–October period. In the LS_1 and LS_2 regions $I\beta_P$ shows a double peak structure with prominent maxima during May–June and October–January for the STC-contaminated cases (in the UT region), while it is very small from May to October for the STC-free case. A significant amount from the abundant ice crystals (of STC) present in the UT region during the summer monsoon period will be lifted up along with air-mass across the tropopause. Consequently, $I\beta_P$ in the lower stratosphere also increases. However, unlike the case during winter, this increase in β_P (or $I\beta_P$) is rather confined to a small region just above the tropopause (the LS_1 region). All the three curves in Figure 15 for the LS_1 and LS_2 regions almost overlap each other during the December to April period. This indicates that the STCs in the UT_2 region during this period did not contribute significantly to $I\beta_P$ in the stratosphere. In general, the influence of STC to the mean backscattering coefficient ($I\beta_P$ /Δh, where Δh is the slab thickness) in LS_1 region is relatively more than that in LS_2, particularly during the summer monsoon period. Thus, presence of dense STC in the UT_2 region (during the summer monsoon period) enhances the particulate scattering in the lower stratosphere, even though this region is practically free from STC.

As lidar data yields reliable β_P values only from the region above the altitude of 'full beam overlap' the effect of STCs below the cloud-base can be examined by studying the scattering property of the medium over a narrow altitude region 8–10 km (UT_1), which is mostly free from STCs (Figure 6b). The mean annual variation of $I\beta_P$ in the UT_1 region for the three cases, (i) when the UT_2 region is STC-free, (ii) the UT_2 region is STC-contaminated and (iii) with both these cases combined, is presented in Figure 15d. Except for the STC-free case, though the $I\beta_P$ in this region also shows an annual variation similar to that for the UT_2 region, the amplitude of this variation is significantly small. Notwithstanding the fact that the values of $I\beta_P$ during the November to April period for the three cases are comparable, for the STC-free condition it shows a decrease during the May–October period. This shows that the presence of dense STCs in the UT_2 region enhances the particulate scattering in the region below the STC-base and the magnitude of this enhancement is much smaller than that in the UT_2 region (where the $I\beta_P$ increases by a factor >20). But when these STCs are thin (optically as well as geometrically), especially during the November to April period, this contribution is almost negligible. Thus, the prevailing STCs in the UT_2 region during the summer monsoon period significantly enhance the scattering from the region above the cloud-top as well as below the cloud-base. The enhancement in particulate scattering in the LS region above the cloud-top could be mainly due to the lofting of STC-particles across the tropopause, which joining with the prevailing LS aerosols modify the volume scattering properties in this region. Though the Brewer–Dobson circulation is weak during summer the troposphere–stratosphere exchange during this period could be aided by an increase in wave activity depending on the prevailing atmospheric condition. Strong convection prevailing over the Indian landmass during the summer–monsoon period, which can transport abundant moisture to the upper troposphere inducing cirrus formation, is also a major source for gravity waves [79].

A study on the influence of STC in the particulate extinction in UT and LS region using SAGE-II data over the Indian longitude sector (70-90°E) from 30°S to 30°N also revealed similar results. However,, as the occurrence of STC is less frequent in the southern hemispheric off-equatorial region, the increase in τ_p in the UT and LS regions due to the influence of STC is relatively small compared to that in the equatorial region [80].

10. Mean latitude variation of the altitude structure of τ_P over the Indian longitude sector

The latitudinal structure of the annual pattern of τ_p in the tropical UTLS region over the Indian longitude Sector is examined using the altitude profiles of particulate extinction at 525 nm obtained from SAGE-II data archive in the latitude region 30°S to 30°N for the period 1998-2005. The profiles are grouped in different latitude bands each having a width of 5°. Contours presenting the annual variation of τ_p in different latitudes bands in the UTLS region are presented in Figure16. The mean annual variation of the altitude of the lapse rate tropopause for each of these latitude bands is superposed on the respective contours.

For the latitudinal region between 0-15°N, the tropopause is cooler (higher) during the December-May period and warmer (lower) during July-October period, in accordance with that reported for tropical locations by prior investigators [67,68]. For the latitudinal sector 15-20°N, the tropopause is higher during April-June and lower during the July-August period. At latitudes > 20°N, a pronounced maximum in tropopause altitude can be observed during the boreal summer and minimum during boreal winter. Though the tropopause altitude varies with latitude, time of the day and day of the year, on an average, this altitude mostly lies in the range 16-18 km.

In general, α_p is relatively large (>10^{-7} m^{-1}) in the UT region for the region north of 20°S. In both the hemispheres α_p shows two peaks. The summer peak (in the respective hemispheres) is more prominent, compared to the winter peak. South of 20°S, α_p in the UT region is relatively small and does not show any pronounced annual variation. The summer-winter contrast in the UT region is almost insignificant beyond 25°S. The winter peak in τ_p becomes relatively weak in the region north of 15°N and becomes almost insignificant beyond 25°N. The summer-winter contrast in α_p is well pronounced beyond 20°N. In contrast to the UT region, the values of α_p in the LS region are relatively small (<10^{-7} m^{-1}), at least by a factor of two. The annual variation of extinction shows a weak summer winter contrast in the LS region for all the latitudinal sectors between 0-30°N. Due to the influence of STCs, which occur at random in different altitudes, the standard error of α_p (expressed as percentages of mean α_p) is generally very large in the UT region. The mean standard error in the attitude region 10-15 km ranges from 20% to 60%. This error decreases progressively with increase in altitude. In the LS region, the error is very small and mostly confined to values in the range 5-15%. In the transition region 15-20 km, the mean error is of the order of 30% which is less than that in the UT region.

Figure 16 shows that the annual variation of α_p in the UT region over the southern hemisphere is distinctly different from that over the northern hemisphere. In this hemisphere high values of α_p (in the UT region) remains fairly confined to latitudes north of 20°S. This difference can

mainly be attributed to the corresponding difference in the pattern of deep convection in these two hemispheres. While the southward migration of ITCZ (during the boreal winter) is fairly confined to latitudes north of 20°S, northward migration (during the boreal summer) extends beyond ~20°N. More over, the convection over the northern hemispheric land mass is much stronger than that over the southern hemispheric oceanic regions. Because of these features, the increase in α_p in the UT region is also confined to the geographical region north of 20°S. The value of α_p in the LS region is relatively small and show similar variations in both the hemispheres. This indicates that the features of aerosol transport in the equatorial (±15°latitude) LS region are fairly symmetric with respect to equator.

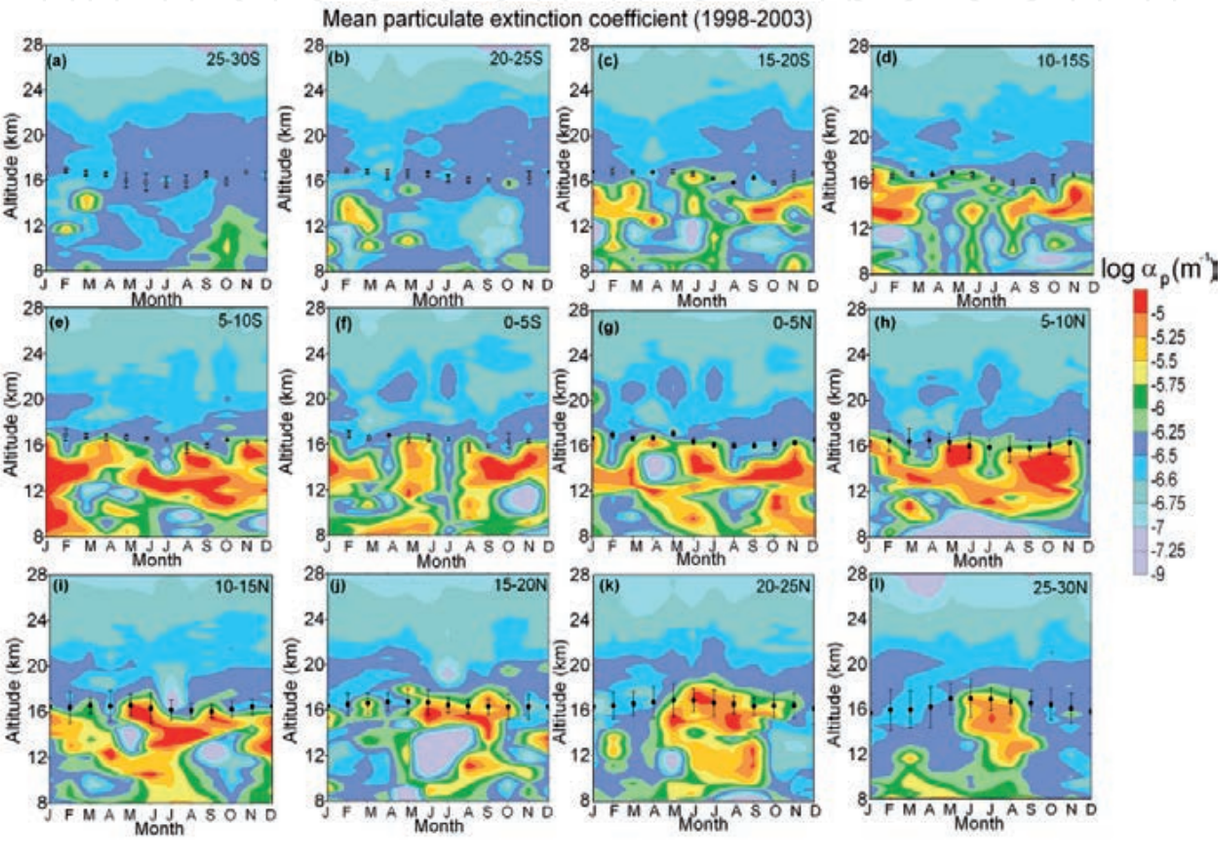

Figure 16. Contour plots showing the mean annual variation of α_p in the UTLS region obtained from SAGE-II in six latitude bands of width 5°from 30°S to 30°N averaged for the longitude region 70°E to 90°E for the period 1998-2005. Month-to-month variation of the mean tropopause altitude for each sector, with vertical bars representing its standard error, is superimposed on the respective contours. For the northern hemisphere the tropopause altitudes are derived from the altitude profiles of temperature obtained from the daily Radiosonde measurements carried out by the India Meteorology Department (IMD) at different locations in each band. For the latitudes south of 5°N, where no Radiosonde measurements are available, the tropopause altitude is obtained from the NCEP data provided along with SAGE-II version 6.2-data archive.

11. Tropospheric convection over the Indian region

The strength of tropospheric convection which can be indexed based on the CAPE could in turn also be related to the thunderstorm activity. The climatology of monthly mean

thunderstorm days (TSD) for the Indian region was studied [63] using the data for the period 1970-1980. The monthly mean values of CAPE at different latitude sectors for the period 1998-2003 over this region is estimated from the respective daily values in each month obtained from the website of IMD (www.weather.uwyo.edu /upperair/ sounding.html). The annual variation of these two parameters for different latitude bands are shown in Figure 17. On an average, the annual pattern of TSD matches well with that of CAPE in all these latitude belts except for the fact that the secondary peak in October is less prominent in CAPE for latitudes north of 15°N. Both these parameters show a significant positive correlation with coefficient exceeding 0.7. Two prominent peaks observed during April-May and October in the near equatorial region merges to become a broad peak in the latitude region 20-25°N (off-equatorial) and subsequently becomes a well defined sharp peak around June-July in the latitude region 25- 30°N. Examining the annual variation of α_p in the light of the annual variation of CAPE/TDS, it can be seen that the occurrence of the high values of α_p (during May and October in Figure 16 h,i, j and those during June, July and August in Figure 16k,l), coincides with the peak in thunderstorm activity (or CAPE) in the respective latitudinal belt. During high convective activity while high values of α_p are observed very close to the tropopause in the latitude belt 0-15°N, significant high values of extinction are observed just above the tropopause in the latitude region between 15-30°N. Intense thunderstorm activity along with deep convection during boreal summer is highly favorable for the formation of dense STCs very close to tropopause leading to an increase in α_p in the UT region. Penetration of particles from these STCs to higher altitudes increases α_p in the LS_I region, as is observed in Figure 16.

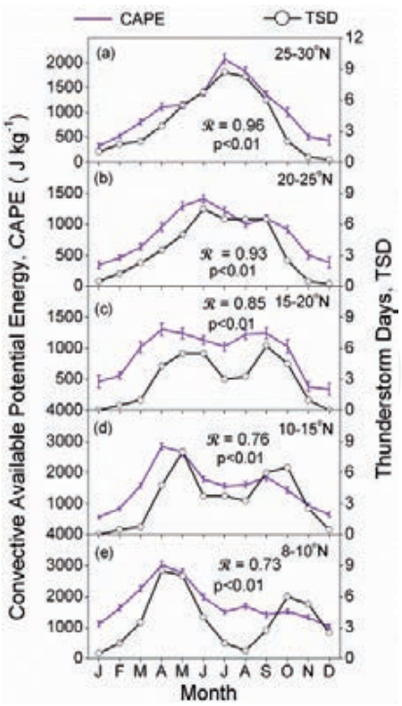

Figure 17. Annual variation of CAPE at different latitude bands over the Indian region along with the mean climatology of thunderstorm days [63]. The vertical bars represent the standard error associated with CAPE. The correlation coefficient (ℜ) between CAPE and thunderstorm days and its level of significance (p) are also shown in respective panels.

12. Influence of dynamics in the latitude variation of particulates in the UTLS region

To delineate the latitude variation of α_P in the UTLS region over the Indian longitude sector (70-90°E), the annual variation of monthly mean τ_P for a latitude band of 5°width in the latitude region 30°S to 30°N, for the three altitude regions 12-16 km (UT), 18-21 km (LS_1) and 21-30 km (LS_2) are examined separately. Figure 18 shows the contour plots of the mean τ_P in the UT, LS_1 and LS_2 regions with month along x-axis and latitude along y-axis. In the UT region, τ_P shows a general decrease with increase in latitude from equator, with its gradient showing a pronounced variation from month-to-month. The summer-winter contrast (with relatively low values during winter and high values during summer) is well discernable in the UT region (Figure 18a). Relatively high values of τ_P observed in the UT region between 15°S-15°N during May to February period are mostly due to presence of dense STCs resulting from the outflow of convective anvils. These are the periods when convective activity in the troposphere is very strong (associated with the southwest and northeast monsoons) in this region. Above 15°N, relatively high values of τ_P are more-or-less confined to the June-August period when the monsoon trough usually reaches its extreme north over the continent. However, beyond 15°S, the values of τ_P decreases significantly with increase in latitude, compared to that observed in the northern hemisphere.

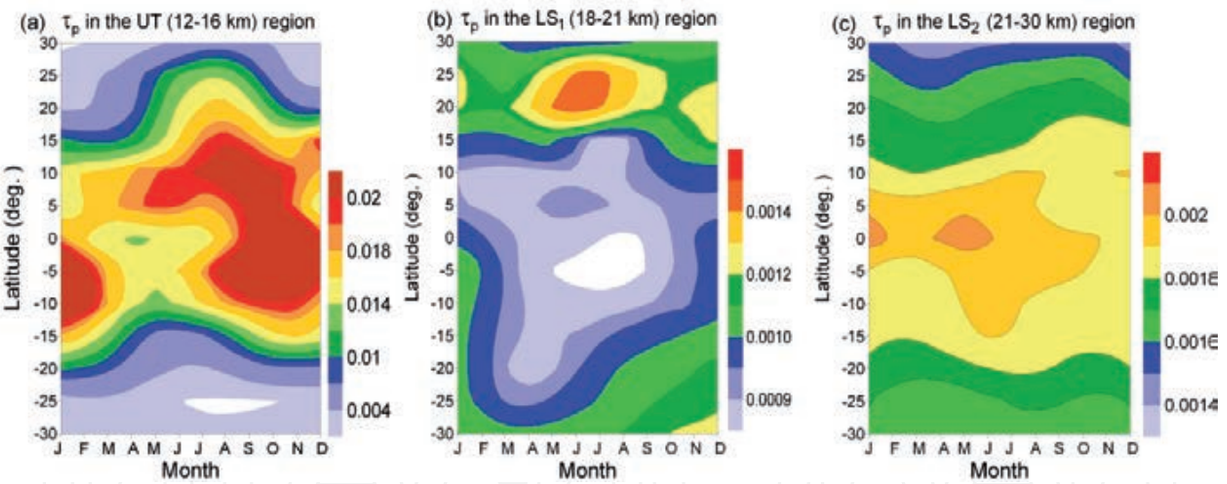

Figure 18. Contour plots showing the latitudinal dependence of the annual variation of τ_P obtained from SAGE-II data in the altitude regions 12–16 km (UT), 18–21 km (LS_1) and 21–30 km (LS_2) for the period 1998-2005.

The latitudinal variation of the annual pattern of τ_P in the UT region shows fairly good correspondence with CAPE and mean thunderstorm activity (Figure 17) over the northern hemisphere. The annual variation of TSD in the latitude region 8-15°N shows two peaks; one during the April-May period and then another during October. Further north, these two peaks get closer and merge to form a single peak in the latitude belt 20-30°N during the June-September period. This corresponds well with the latitudinal variation of the annual pattern of τ_P in the UT region (Figure 18a). Increase in convective activity (as well as convective outflow) over the Indian region associated with the northward migration of

ITCZ along with the development of deep convection over the Bay of Bengal (particularly over its northern parts) during this period aid the formation of abundant dense STCs in the UT region. The annual variation of high altitude cloud amount over the Indian region also shows the presence of large deep convective cloud systems reaching very high altitudes and even penetrating the tropopause has been reported [81]. As the strength of the tropospheric convection decreases significantly during winter and the ITCZ shifts to the southern hemisphere sector, the probability of occurrence of dense STC over the southern hemisphere increases significantly. The deep convective clouds over this region get confined to a small geographical region between equator and 10°. Most of the STCs occurring over the Indian region during this period will be of *in situ* origin [78]. These clouds will be either ultra-thin or sub-visual type cirrus with very low values of optical depth (<0.03).

The latitude variation of the annual pattern of τ_P in the LS_1 and LS2 regions are presented in Figure 18b and Figure 18c respectively. In general, the mean τ_P in the LS_1 (18-21 km) region is in the range of 0.0008-0.003, which is one order in magnitude less than that in UT. In this altitude region, τ_P clearly shows relatively high values in the off-equatorial (north of 15°) regions and low values in the equatorial regions. Studies [82] on stratospheric aerosol optical depth during the decay phase of the volcanic aerosol at mid-latitudes using SAGE-II data have shown the presence of sinusoidal variation in the aerosol optical depth superimposed on an exponential decay with maximum and minimum occurring during the local winter and summer respectively. Over tropics the amplitude of these oscillations are significantly small and hence gets submerged in the disturbances caused by subsequent minor volcanic eruptions. As the period selected for the present analysis is volcanically quiescent, these oscillations are well discernable over the tropics. In the region 10-15°N, the annual variation of τ_P shows a relatively high value during winter and low value during summer. Note that, this variation is very similar to the annual variation of particulate backscatter observed in the lidar data from Gadanki [7]. Above 15°N, high values of τ_P are observed in the LS_1 region during the May-August period centered around 20-25°N. The particulate extinction just above the tropopause also shows a significant enhancement in the latitude region between 20-25°N (Figure 18b). This could be due to the penetration of the top of the high altitude semitransparent cirrus clouds above the cold point (tropopause). The two peaks observed in CAPE (and TSD) near equator (Figure 17) during April and October becomes more prominent and gets closer with increase in latitude (towards north) and merges to become a strong broad peak centered around July. This shows that the convective activity in the 20-30°N is very strong and the outflow occurs very close to the tropopause. The frequency of occurrence of cloud top altitude (observation from CALIPSO) shows a maximum value of 17±0.5 km in this latitude region during the June to September period which is at least 1 km larger than the maximum value observed at other latitudes (between 30°S to 30°N) at any period [81]. Thus convection over the Indian land mass during the summer monsoon period in the 20-30°N latitude band is the strongest one in the entire latitude region 30°S to 30°N at any time during the year. This is a characteristic feature for the Indian longitude region. Strong convection plays a major role in transporting particulates from the upper tropospheric cirrus cluster to lower stratosphere causing a pronounced increase in τ_P in the LS_1 region. Note that, such a feature in convection and

hence in τ_P (in the LS_1 region) is not observed in the southern hemisphere. In LS_2, τ_P shows a distinct latitude variation with relatively high values near the equator up to 15° in both the hemispheres and low values over the off-equatorial regions (>15°). Relatively high values of τ_P are observed in the LS_2 region during the January-June period in the latitude region 15°S-10°N and low values during the rest of the period. This pattern slowly reverses with increase in latitude. Beyond 10°N, τ_P shows a pronounced winter peak with low values during the March-May period. The annual variation of τ_P in the LS_2 region over the southern hemisphere is quite similar to that in the northern hemisphere. High values of τ_P observed between 15°S and 15°N in the LS_2 region confirms the presence of a Tropical Stratospheric aerosol Reservoir (TSR) during the study period. Earlier studies carried out by several investigators [29,83] revealed the presence of this band structure (with high aerosol loading) in the 21- 30 km altitude region over the equatorial region during volcanically perturbed period. Examining the aerosol climatology in the LS region using the SAGE-II data both during the volcanically perturbed period as well as during the near background conditions, *Bauman et al.* [84] reported maximum aerosol optical depth near the tropics and minimum between 15-45°◉latitudes. *Trepte and Hitchman* [28] were the first to propose the existence of a low-latitude maximum in lower stratospheric aerosol optical depth which they referred to as the 'tropical aerosol reservoir'. They also examined the post-volcanic aerosol distribution in tropics and observed that the 18-21 km (LS_1) region experiences a rapid pole ward transport, while in the upper regime (LS_2) aerosol lofting and subsequent accumulation occurs within 20°S-20°N. This can fairly well explain the observed low values of τp in the lower regime (LS_1 region) and high values in the upper regime (LS_2 region) in the equatorial region between 15°S to 15°N in the present study. The variation of τ_P in the UT region in both these hemisphere are more-or-less complementary to each other indicating similar seasonal dependence in both the hemispheres, except for the fact that decrease in τ_P with increase in latitude (from equator) towards south is much faster than that in northern hemisphere. This is quite expected because the southern hemispheric sector is mostly occupied by ocean. The seasonal influence is rather insignificant in the LS_1 and LS_2 regions.

13. Influence of moderate volcanic eruptions on α_p in the LS region

The background stratospheric aerosol layer usually referred to as the Junge layer [85] consists of liquid droplets composed of a mixture of sulfuric acid and water. This layer will be quite prominent subsequent to major volcanic eruptions, such as El Chichón (Mexico, 1982) and Mount Pinatubo (Philippines, 1991), which are powerful enough to inject large amount of SO2 into the stratosphere [86]. After oxidation, sulfate aerosols are formed at these altitudes. These particles are subsequently distributed globally depending on the latitude of the eruption. Removal of these aerosols is rather difficult. It takes several months to years (depending on size) to scavenge these volcanic aerosols. The last major eruption (Mount Pinatubo) took place in 1991 and the stratospheric aerosol layer returned to its "background" level around 1997. There is no major increase in stratospheric aerosol loading after 1997 [13,25]. However, increase in the anthropogenic SO2 emission has been proposed as a plausible mechanism responsible for the observed small increasing trend in

stratospheric background level in the recent past [26]. An overview of the current understanding on stratospheric aerosol science can be found in *Thomason and Peter* [24].

Though, in general, most of the particles generated through the gas-to-particle conversion process in the stratosphere will be small and nearly spherical in nature, there could be a few larger size particles in the lower stratosphere associated with moderate and intense volcanic eruptions, leading to a pronounced enhancement in δ and α_p in this region. These volcanic perturbations are clearly distinguishable from STCs in the UT region based on the amount of enhancement, its temporal structure as well as the duration of enhancements. Moreover, while δ (and α_p) of STCs vary significantly at shorter time scales [57,87], the stratospheric cloud formed through volcanic emissions will be stable for a longer period. In addition, the values of δ associated with STC will be significantly larger (as they are mostly composed of non-spherical ice crystals) than those of volcanic clouds. The vertical structure of δ for the volcanic cloud will remain fairly stable at short time scales typically over a night. Thus a long lasting enhancement of δ in the LS region observed by the lidar is an indicator for assessing the volcanic impact on stratospheric aerosols. In order to illustrate this in detail and depict the difference in the nature of perturbations due to STC and volcanic cloud, a contour map of δ for a typical night (25 November 2002) during the eruption period of Reventador (started in November 2002 and lasted up to January 2003) is presented in Figure 19a. In order to accommodate the large variations, the contouring of δ in this figure is performed in two bands; one from 0.04 to 0.2 in steps of 0.02 and the other above 0.2 at 0.2 interval. Two enhanced layers (of δ) one between 15 and 16 km and the other around 19km, are distinctly seen in this figure. The value of δ and its temporal variations are very large for the lower layer while these are very small for the upper layer. The lower layer disappears after mid-night while the upper layer continues to persist up to the end of lidar observations. This shows that the lower layer is an STC while the upper one is the volcanic cloud. This volcanic cloud will persist on subsequent night also while STC may or may not

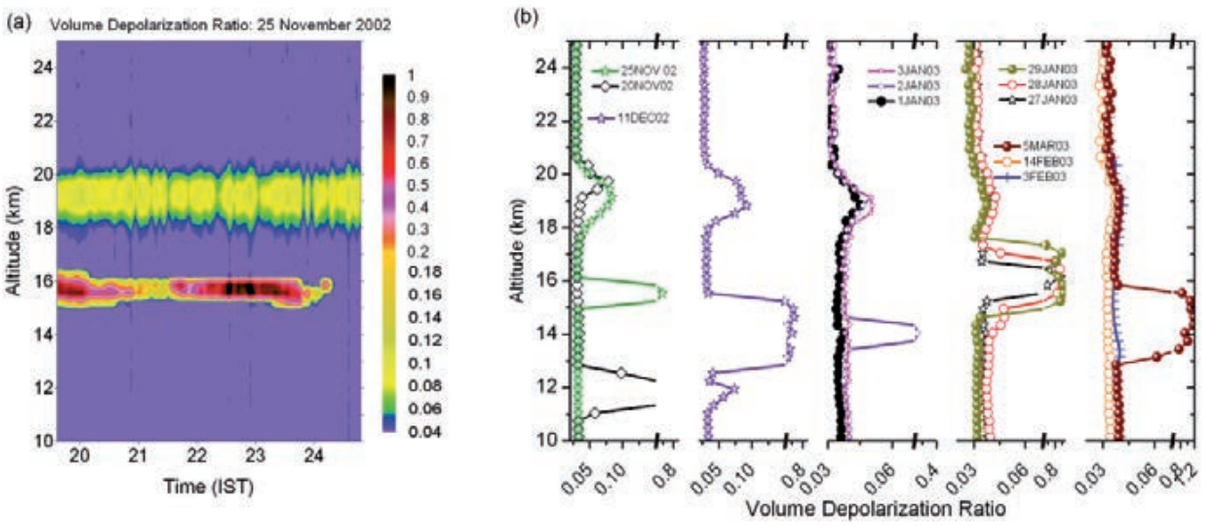

Figure 19. Altitude- cross-section of volume depolarization ratio (δ) during the night of 25 November 2002 (a). Altitude profiles of δ on different nights (averaged for one hour around 22:00 IST) for the period November 2002 to March 2003, during the active and post -active phases of Mt. Reventador (b).

be present. To illustrate this the sequences of lidar profiles observed on a few nights during the eruption period of Reventador are presented in Figure 19b.The features of the layer located around 19 km (in the LS region) is rather steady in all these profiles while those of the layer below ~17 km (due to STC), is highly variable. The stratospheric layer is strongest in December and started decaying in January 2003 and became almost insignificant by March 2003, while the STC layers appear at random.

The perturbation in the lower stratosphere over the equatorial and off-equatorial regions during the period 1998-2005, when the volcanic activity was relatively small, are examined in detail [88] using the altitude profiles of α_p over the tropics from SAGE-II data archive (Figure 20a) and the altitude profiles of α_p and δ obtained from lidar data (Figure 20b and 20c) at Gadanki. Zonal-averaged monthly mean α_p at different altitudes in the lower

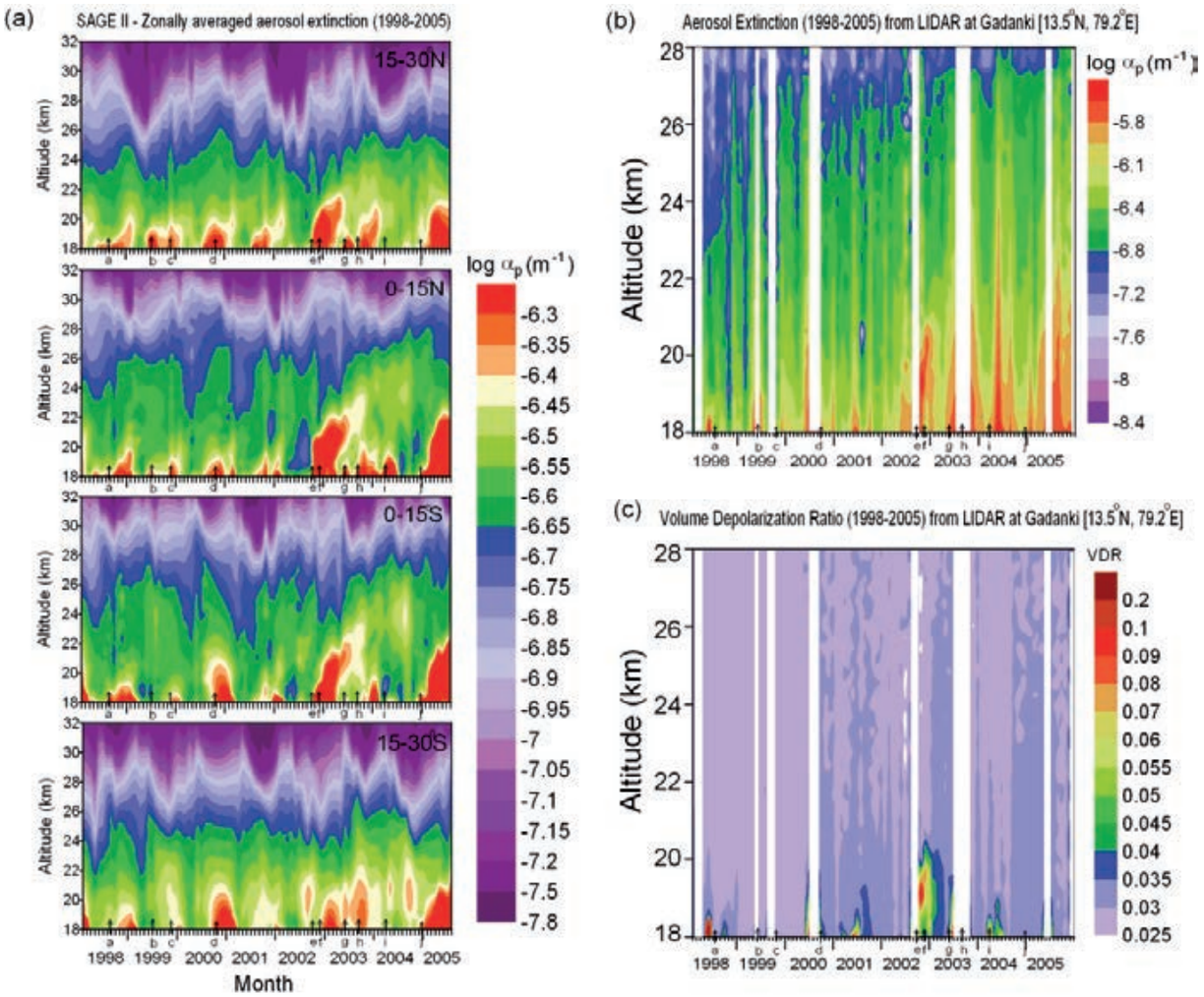

Figure 20. (a) Zonally averaged monthly mean extinction coefficient (α_P) for the equatorial (0°S–15°S and 0°N–15°N) and off-equatorial (15°N–30°N and 15°S–30°S) regions estimated from SAGE-II data, (b) altitude-time cross section of aerosol extinction coefficient (α_P) from lidar and (c) altitude-time cross section of the Volume Depolarization Ratio from lidar (at Gadanki) during the period 1998–2005. The letters along the abscissa represent the eruption of each volcano, the name and other details of which are listed in Table 1. The major ticks correspond to December of each year.

stratosphere for four different latitude belts (over tropics) are used mainly to have sufficient number of profiles in each belt as well as owing to the fact that in the lower stratosphere the spatial variability along longitude could be minimal (because of efficient mixing in the zonal direction and strong horizontal transport prevailing in the region). As expected the aerosol extinction decreases with increase in altitude with significant loading confined to the altitude region 18–27 km. Short-lived enhancement in α_P are distinctly seen in the lower stratosphere (Figure 20a) in different years. These signatures could be attributed to the influence of various minor volcanic eruptions during the study period. Those eruptions which could make discernable impact in the stratosphere are marked at the start of the respective eruption along the X-axis of each panel and further details of these eruptions are summarized in Table 1. Only those eruptions which occurred between 30°S and 30°N are included in Table 1. The Volcanic Explosivity Index (VEI) for different eruptions [89] is obtained from the Web site of Smithsonian Institution–Global Volcanism Program (GVP). The eruptions of Ulawun (eruption d), Ruang (eruption e), Reventador (eruption f), and Manam (eruption j) are relatively strong with VEI ~4 (Table 1), and the signature of these eruptions are well discernable in the lower stratospheric (18–20 km) aerosol extinction (Figure 20a). These perturbations can be distinctly seen both over the equatorial as well as off-equatorial regions.

			Duration		Location		
Identification Letter	Volcano	VEI	Start	End	Latitude (deg)	Longitude (deg)	Altitude (m)
a	Guagua-Pichincha	3	August 1998	May 2001	−0.17	−78.6	4784
b	Mayon	3	June 1999	March 2000	13.3	123.7	2462
c	Tungurahua	3	October 1999	January 2009	−1.5	−78.4	5023
d	Ulawun	4	September 2000	November 2000	−5.0	151.3	2334
e	Ruang	4	September 2002	September 2002	2.3	125.4	725
f	Reventador	4	November 2002	January 2003	−0.08	−77	3562
g	Anatahan	3	May 2003	July 2003	16.4	145.8	790
h	Lokon-Empung	3	September 2003	September 2003	1.4	124.8	1580
i	Soufrière	3	March 2004	May 2004	16.7	−62.2	915
j	Manam	4	October 2004	May 2009	−4.1	145.0	1807

Table 1. Details of volcanic eruptions in the tropics during 1998–2005 having significant stratospheric impact

Figure 20b shows the temporal variation of the altitude structure of α_P obtained from lidar during the period 1998– 2005 in the form of a contour plot. This figure also depicts the signatures of various minor volcanic eruptions similar to that depicted in the zonal mean values obtained from SAGE-II data, in the latitude sector 0–15°N (Figure 20a). Small-scale features are more pronounced in lidar data (Figure 20b) mainly because of the fact that it corresponds to a point observation while that in Figure20a is the zonal average. In volcanically quiescent periods the sulfur bearing gases, SO2 and OCS emitted from the earth's surface are transported across the tropopause [90], photolyzed, and oxidized to sulfuric acid before condensation to form sulfuric acid and water droplets in the stratosphere [24,91], which are, by their liquid nature, spherical. The depolarization caused by these particles will be very small and hence the resultant δ in the stratosphere will be

very close to that of the molecules. In general, it is in the range 0.03 to 0.04. But, during major volcanic eruption abundant amount of precursor gases will be injected into the lower stratosphere along with a few fine particulates. Because of this influx of particles and gases there will be an increase in the number density of particles as well as an increase in the size of these particles. The size spectrum of the stratospheric particles also shifts toward the larger size regime following the volcanic eruption [92]. As some of those particles that are directly injected into the lower stratosphere during volcanic eruption could be non-spherical in nature, an increase in δ in the stratospheric aerosol would be expected.

Figure 20c shows a contour plot of δ at different altitude in the lower stratosphere over Gadanki during the period 1998–2005. This plot generated adopting the same procedure as that used for generating Figure 20b from α_p profiles, clearly shows a few short-lived δ enhancements in the lower stratosphere. The sporadic increase in δ is associated with the eruption of a few moderately intense volcanic eruptions. The duration of the increase in α_p also matches well that of δ. The disturbances caused by eruption of volcanoes Ruang (eruption e) and Reventador (eruption f) are relatively stronger (δ ranging from 0.05 to 0.2 in the altitude region 18–21 km during November 2002 to February 2003). In a few cases the enhancements in α_p and δ does not match exactly. This could be due to the fact that the volcanic locations are at different distance from Gadanki as well as the prevailing transport process could be different at various occasions.

14. Long term variations of τ_p in the LS region

Zonal mean values of τ_p in the altitude region 18–28 km averaged for the four latitude belts, each of width 15°, in each month are used to examine the temporal variations in both the hemispheres. Time series plots of these for the equatorial (0–15°S and 0–15°N) and off-equatorial regions (15–30°N and 15–30°S) are shown in Figures 21a and 21b, respectively, along with a similar plot of τ_p obtained from lidar at Gadanki in Figure 21c. In the equatorial region the temporal variations in τ_p are very similar in both the hemispheres. The mean level of τ_p shows an abrupt increase after 2002 [88] though the oscillations around this mean level is fairly similar to those before 2002. Over the off-equatorial regions the mean level of τ_p shows a rather steady (gradual) increase from 1998 to 2005. A sharp increase in τ_p is observed towards the trailing edge of the data in the year 2005. During the period 1998–2002, the value of τ_p in the equatorial region is a minimum and is close to ~0.0025. The mean τ_p in the altitude region 18–28 km obtained from lidar at Gadanki also shows similar feature as that observed from SAGE-II over the equatorial region. In general the value of τ_p in the LS region obtained from lidar data is larger than that obtained from SAGE-II. This could be due to the fact that the lidar observation is a single point measurement while the SAGE-II data used in this analysis is zonally and meridionally averaged for the equatorial and off-equatorial regions.

All the plots in Figure 21 show a general increasing trend in stratospheric particulate (aerosol) optical depth during the period 1998–2005 in addition to the periodic variations. On the basis of lidar observations during the period 2000–2009, a similar increase in the integrated stratospheric backscatter coefficient (in the altitude region 20–25 km) at the rate

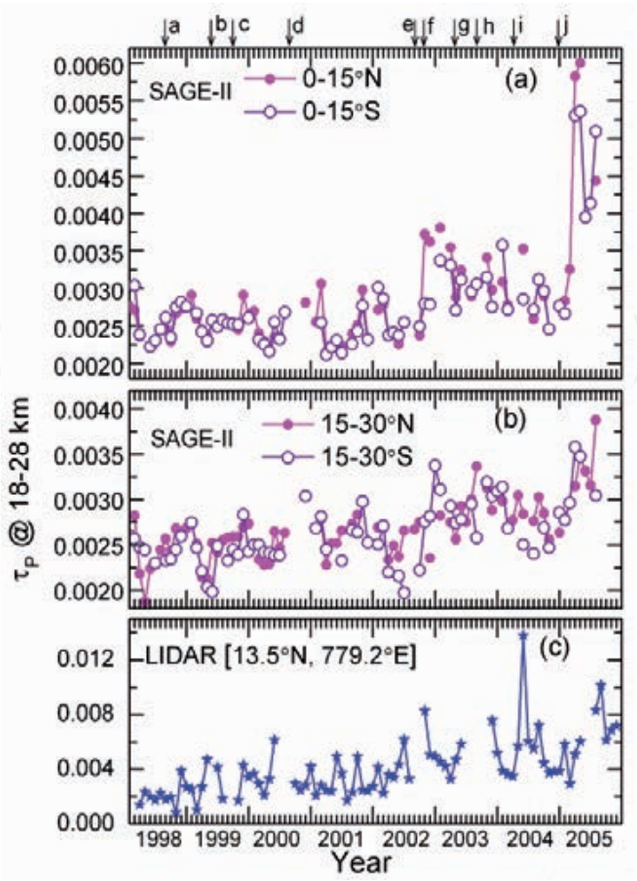

Figure 21. Time series of zonal mean monthly average τ_P in the altitude region 18–28 km obtained from SAGE-II for (a) the equatorial region (0°–15°N, 0°–15°S) and (b) the off-equatorial region (15°–30°N and 15°–30°S), along with (c) the mean τ_P obtained from lidar at Gadanki.

of 4.8% and 6.3% per year (with respect to its value in 2002) was reported [26] at Hawaii (19.5°N, 155.6°W) (Mauna Loa Laboratory) as well as at Boulder (40°N) (Colorado). The increase in τ_P at Hawaii and Boulder was attributed to the increase in global coal consumption since 2002, mainly from China, and subsequent increase in emission of SO2. Anthropogenic aerosols produced through gas-to-particle conversion of precursor gases like sulfates and ammonia transported to the upper troposphere [5] through intense convection [93] in the tropics and subsequently across the tropopause also could possibly be a contributing factor for this increase. An increase in tropical upwelling (Brewer- Dobson circulation) because of global warming also was suggested to be a plausible mechanism for the observed increasing trend [93,94] in stratospheric β_P after 2002.

Even though on an average the stratospheric particulate loading is in its background level during the period 1998–2005, it was influenced particularly by a few moderate volcanic eruptions mainly after September 2002. While the period before September 2002 was absolutely quiet (with low particulate loading), the later period was mildly disturbed. The variation in stratospheric particulate loading need not solely be represented by a corresponding variation in tephra emissions Their could be some other causative mechanisms, such as increase in anthropogenic emissions as well as the increase in tropical upwelling, which could influence the stratospheric particulate loading.

15. Periodic variation of τ_p in the LS region

In addition to the general increasing trend, the values of τ_p in Figure 21 shows a seasonal cycle with winter maximum and summer minimum modulated by a long-period oscillation. These oscillations could primarily be due to the influence of large-scale atmospheric waves. The time series data of τ_p is spectrum analyzed to bring out the characteristics of the prevailing periodic variations. Before subjecting the data to spectral analysis, the linear trend is removed from the original data. The residual part is Fourier analyzed and the resulting amplitude spectra for different latitude bands (0–15°N, 0–15°S, 15–30°N and 15–30°S) are presented in Figures 22a and 22b. These amplitude spectra reveal the presence of a strong annual component (~12 months) along with a quasi-biennial component (~30 month) both in the equatorial and off-equatorial regions [88]. The spectral amplitude of QBO is as strong (significant) as that of annual oscillation (AO). Figure 22c shows the amplitude spectrum obtained from the lidar derived values of τ_p (at Gadanki). Even though Figure 22c shows more significant peaks in the short-period regime, the spectral amplitude is more pronounced for semi-annual (SAO) and annual (AO) components. This spectrum also shows a secondary peak around 46 months followed by troughs at 23 and 92 months. The spectral amplitude for 30 month periodicity is larger than those at the troughs on either side of this secondary peak. Though the period for the peak amplitude (46 months) is much larger than that expected for the stratospheric QBO, on the basis of the inference derived from Figures 22a and 22b, as well as owing to the fact that the spectral amplitude at 30 months is not a minimum, the characteristics of the 30 month periodicity is examined in the later part to

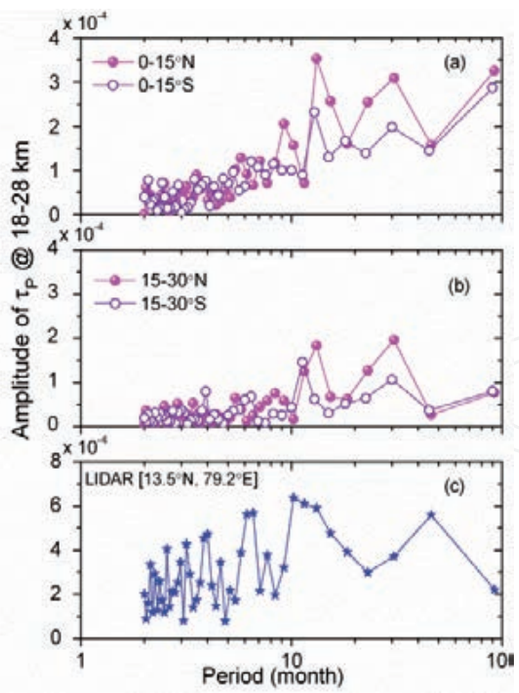

Figure 22. Amplitude spectra of τ_P in the altitude region18–28 km during the period 1998–2005 derived from the time series of zonal mean monthly average τ_P in this altitude region obtained from SAGE-II data for (a) the equatorial region and (b) the off-equatorial-region, along with (c) that obtained from lidar data at Gadanki

delineate its altitude structure in the lidar data. The SAGE-II data did not show the signature of SAO, which could be due to the inherent smoothing out of this component while taking the zonal mean. The higher spectral amplitude of AO compared to that of QBO is quite expected (as it is true for the wind field also).

16. Quasi-biennial oscillations in τ_p and zonal wind in the LS region

For this study the high resolution Radiosonde data of zonal wind in the lower stratosphere from an equatorial station (where the quasi-biennial oscillation, QBO, signature is expected to be maximum), Singapore (1°22″N, 103°55″E), obtained from Web site http://www.geo.fu-berlin.de/en/met/ag/strat/produkte/qbo/ are used. The time series data of monthly mean zonal wind at Singapore at 20 hPa and 30 hPa levels during the study period are presented in Figure 23. This figure shows that the quasi-biennial oscillation in zonal wind (QBO_U) is in the easterly phase during the 1998, 2000–2001, 2003 and 2005. The westerly phase during 1999 and the easterly phase during 2000–2001 are relatively broad. Different phases of QBO_U are indentified from this time series to study the influence of QBO_U in lower stratospheric aerosols.

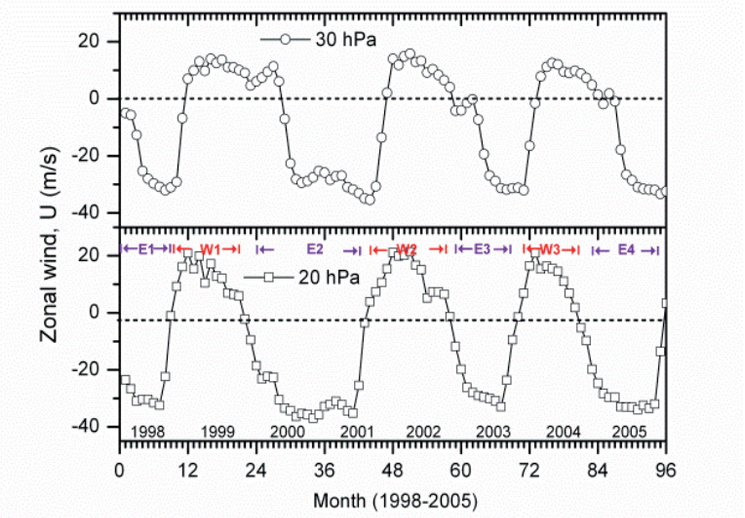

Figure 23. Time series of monthly mean zonal wind at Singapore at 20 and 30 hPa levels during the period 1998-2005. E_1, E_2, E_3, and E_4 are the periods in which QBO_U was in its easterly phase, and W_1, W_2, and W_3 are those in which QBO_U was in its westerly phase.

16.1. Latitude variation of τ_p in LS region over the Indian longitude sector in two different phases of QBO_U

The latitude variation of τ_p in the altitude range 21–28 km in the band 0–30°N (averaged for every 5°) over the Indian longitude sector (70–90°E) is examined during the consecutive easterly and westerly phases of QBO_U in 1998 and 1999 separately. Figure 24 shows the latitudinal variation of τ_p during these two phases of QBO_U. This mean τ_p is obtained by averaging the particulate optical depth in individual months when the QBO_U phase has reversed completely (the wind speed has reached its highest value). While the value of τ_p is

relatively high during the westerly phase of QBO_U in the equatorial region up to 15°N, relatively high values are observed during the easterly phase of QBO_U in latitudes beyond 15°N. The lidar derived τ_p is relatively low during the easterly phase of QBO_U compared to that during its westerly phase. This is in good agreement with that from the latitude variation of τ_p for these 2 years derived from SAGE-II data.

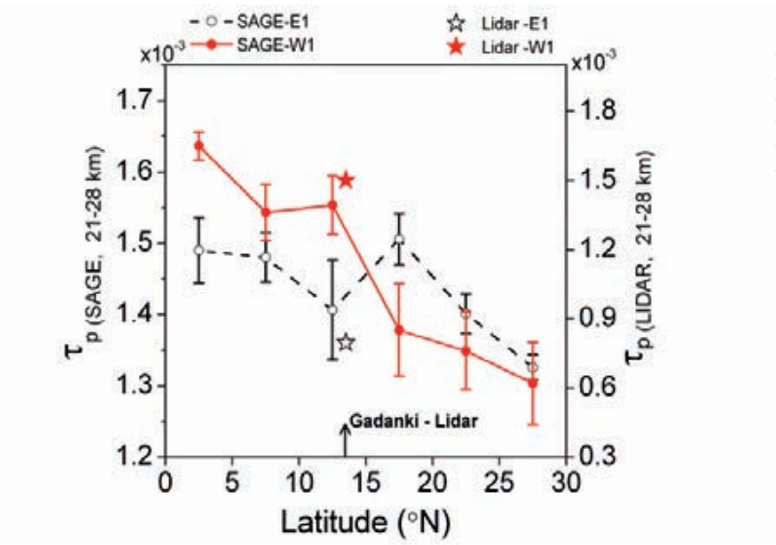

Figure 24. Latitude variation of mean τ_p in the altitude region 21–28 km obtained from SAGE-II averaged over the longitude sector 70°–90°E during the easterly phase (E_1) and westerly phase (W_1) of QBO_U in 1998 and 1999, respectively (vertical bars represent the standard error). The open star represents the value of τ_P during the easterly phase of QBO_U (1998), and the red star represents that during the westerly phase (1999) for the altitude region 21–28 km obtained from lidar at Gadanki (marked on the X- axis by a vertical arrow), the scale of which is shown on the right-hand side of the plot.

The value of τ_p shows a pronounced decrease with latitude during westerly phase of QBO_U compared to that during its easterly phase. Interestingly, during the easterly phase of QBO_U, while the latitude variation of τ_p is relatively small in the equatorial region (0– 15°N), beyond 20°N it decreases sharply with increase in latitude. By examining the altitude profile of backscatter ratio obtained from lidar data at Mauna Loa at Hawaii (19.5°N, 155.6°W), Barnes and Hofmann [11] reported an enhancement of backscatter ratio (enhanced aerosol loading) in the altitude region 21–30 km during the easterly phase of QBO_U. This feature agrees well with the above observation derived from the latitude variation of τ_p at Hawaii.

16.2. Latitude variation of zonal mean τ_p in the LS region over the tropics in different phases of QBO_U

On the basis of the measured particulate loading in the stratosphere, out of the 8 year period considered for the present analysis, the period 1998–2002 was absolutely quiescent while the period 2003–2005 was mildly disturbed. The variation of zonal mean τ_p in the latitude region 30°S to 30°N (averaged for every 5°) in the alternative easterly and westerly phases of QBO_U during the volcanically quiescent and mildly disturbed periods are presented in Figures 25a and 25b respectively. As seen from Figure 23 during the study period (8 years) the QBO_U

completes approximately 3.5 cycles, with two easterly (E_1 and E_2) and two westerly (W_1 and W_2) phases during the period 1998–2002 and two easterly (E_3 and E_4) and one westerly (W_3) phase during the mildly disturbed period of 2003–2005.

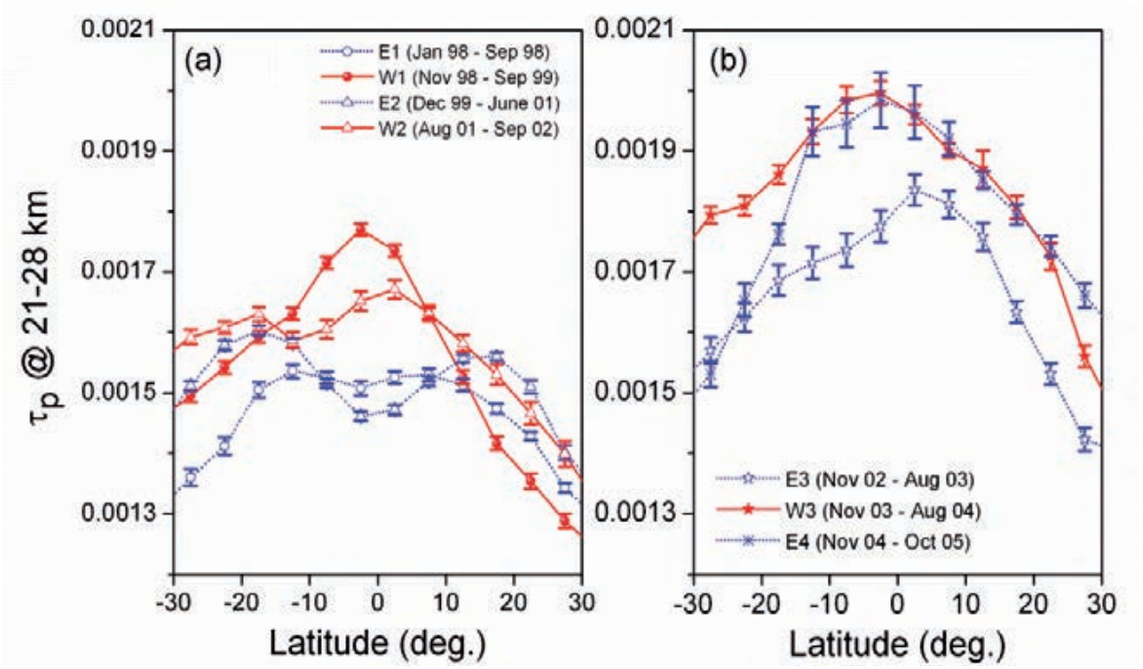

Figure 25. Latitude variation of zonal mean τ_p in the altitude region 21–28 km from 30°S to 30°N obtained from SAGE-II during the alternate easterly and westerly phases of QBOU during the (a) absolute quiet period (1998–2002) and (b) mildly disturbed period (2003–2005). Vertical bars show the corresponding standard error

During the former half (very quiet period), the mean τ_p in the equatorial region shows a general enhancement during westerly phase of QBOU (W_1 and W_2) while in the off-equatorial region of northern hemisphere it shows an enhancement during the easterly phase of QBOU [88]. When the stratospheric QBOU was in its westerly phase the mean values of τ_p in both the hemispheres decreases steeply with increase in latitude on either side of equator. During the easterly phase of QBOU, though the value of τ_p decreases with increase in latitude beyond 15°N, it is fairly uniform in the equatorial region (15°S to 15°N) with a bite-out over the equator. During the latter half (mildly disturbed period), the mean τ_p decreases rapidly on either side of equator with increase in latitude in both the phases of QBOU. Figure 25b shows a general enhancement in τ_p during W_3 period in the equatorial and off-equatorial regions of both the hemispheres compared to that during the E_3 period. However, during E_4, τ_p in general is relatively large in the equatorial and northern hemispheric off-equatorial region compared to that during E_3 and W_3. Note that, in the above analysis two consecutive easterly and westerly cycles of QBOU are considered and the inferences arrived based on the latitudinal structure of τ_p in these two phases. The inference may apparently be contradicting if one considers the other two pairs, westerly of the first pair and easterly of the next (eg W_3 and E_4), particularly during the mildly disturbed phase of 2003–2005 (Figure 25b). This is mainly due to the fact that the background τ_p has a strong

increasing trend during this half in addition to the periodic variations. This can override the periodic variations associated with QBOU. However, this contradiction is totally absent in the former half (1998–2002) when the background τ_p was fairly steady. During this period τ_p in the equatorial region is high in both the westerly phases (W_1 and W_2) compared to that during the easterly phases E_1 and E_2, irrespective of sequence of pairs considered. This shows that the influence of QBOU in τ_p can be clearly delineated only during the very quiescent volcanic periods, when the background stratospheric aerosol loading remains in its steady background level.

16.3. Altitude structure of α_p in the lower stratosphere in different phases of QBOU

Figure 26a shows the mean profile of α_p in the altitude region 18–28 km obtained from lidar data at Gadanki for the two periods, January to September 1998 and November 1998 to September 1999, when the QBOU was in its easterly and westerly phases, respectively. Figure 26a clearly shows that the value of α_p is consistently larger during the westerly phase of QBOU than the corresponding values during its easterly phase. This shift in the altitude profile toward a higher value side during the westerly phase is not due to the influence of any trend because the mean level of the stratospheric particulate optical depth in the 0°–15°N region remains fairly the same during the period 1998–2002 and an increase in this level occurred only after 2002 (Figure 21).

For a more detailed study on the effect of QBOU on stratospheric aerosols, the zonal mean altitude profile of α_p in different phases of QBOU during the study period is examined for

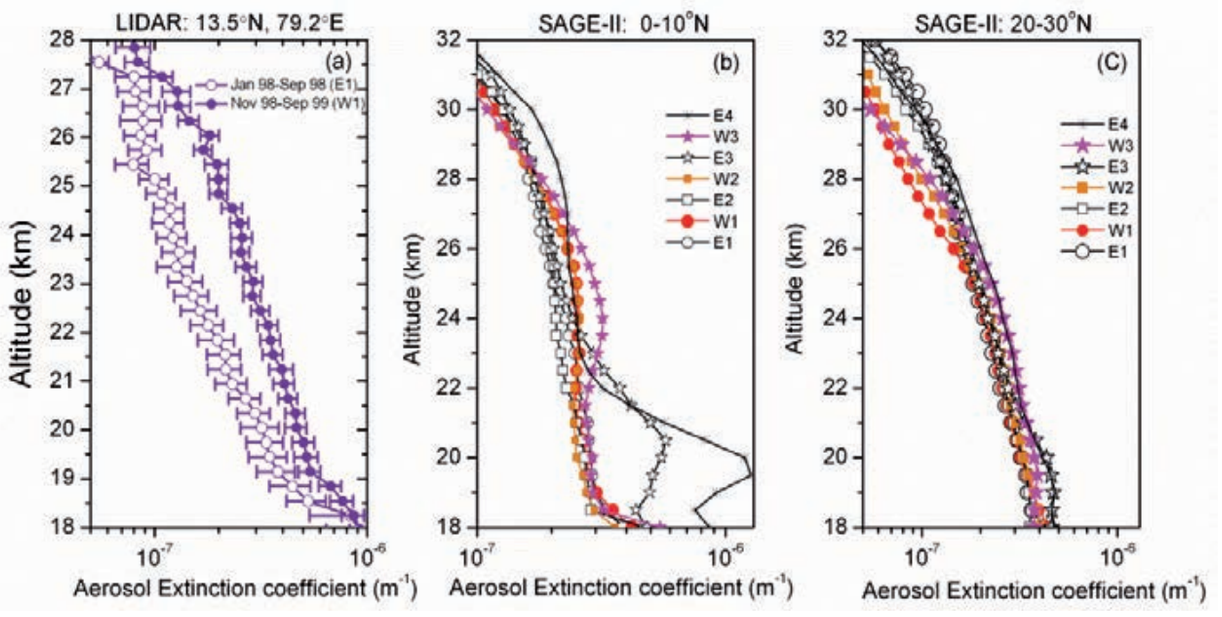

Figure 26. Altitude profiles of mean extinction from lidar at Gadanki for the E_1 and W_1 phases of QBOU for the period 1998-1999, along with the altitude profiles of zonal mean extinction from SAGE-II during the four alternate phases of QBOU from 1998-2005, averaged over the latitude regions (a) 0°N–10°N and (b) 20°N–30°N, representative of equatorial and off-equatorial region

the equatorial and off -equatorial regions separately. The mean profiles thus obtained for the latitude region 0–10°N and 20–30°N (averaged zonally, as well as along the respective latitude bands) are shown in Figures 26b and 26c, respectively. Over the equatorial regions the altitude profile of aerosol extinction coefficient in the altitude region 22–27 km during the easterly phase of QBO_U are consistently lower than that during the subsequent westerly phase. In the off-equatorial region, the aerosol extinction coefficient in the altitude region 25–32 km is found to be relatively low during the westerly phase. It may be noted that the earlier studies also have shown that aerosol extinction in the lower stratosphere can be influenced by the phase of the quasi biennial oscillation [11,28,29,95] in this region even though the difference in the nature of the latitudinal dependence over the equatorial and off-equatorial regions were not addressed in detail.

Association between the altitude structure of QBO in particulate extinction (QBO_a) and QBO_U for the entire study period is examined by subjecting the time series of zonal mean monthly average α_P (obtained from SAGE-II) and zonal mean zonal wind, U (obtained from NCEP reanalysis), at each altitude bin from 20 to 30 km to Fourier analysis after removing the linear trend. To illustrate the QBO features, the spectral components corresponding to the periods other than 22-45 month are removed from the respective trend removed time series data using the corresponding amplitudes and phases. The altitude structure of the residual amplitudes thus obtained for α_p and U over the equatorial and off-equatorial regions are presented in Figure 27. The left side panels show the residual amplitude for α_p and the right side panels the same for zonal wind. Both these panels show clearly the presence of a QBO. While the phase of the biennial oscillation in wind shows a clear downward propagation with time as expected, the phase of QBO_a changes many times with increase in altitude. This change in the phase of QBO_a with altitude is analogous to that reported for the stratospheric ozone [96] and was attributed to the secondary meridional circulation (SMC).

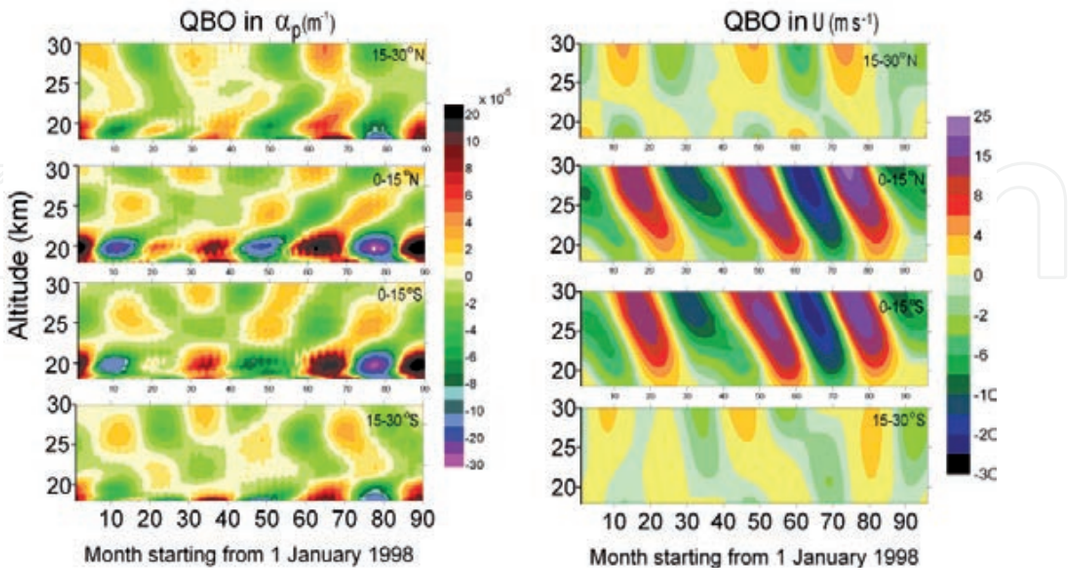

Figure 27. Amplitude spectra of QBO in α_P (from SAGE-II) and zonal wind (from NCEP) for the altitude region 20 to 30 km showing the time history of the biennial component for the period 1998 - 2005 for the equatorial and off-equatorial regions.

17. QBO in α_p and secondary meridional circulation

To study the altitude structure of the QBO_a, the time series of zonal-averaged monthly mean aerosol extinction coefficient at different altitudes (at 0.5 km interval) are subjected to Fourier analysis after removing the linear trend. This analysis of α_p at different levels showed a prominent peak in its amplitude corresponding to the periodicity of QBO (30 month) and AO (12 month). Figure 28 shows the altitude profile of the amplitude and phase of QBO_a from 18 to 32 km in the equatorial (0–15°N and 0–15°S) and off-equatorial (15–30°N and 15–30°S) regions. In general, the amplitude of QBO_a decreases with increase in altitude (as that observed in the raw aerosol extinction data). Over the equatorial region, the altitude variation of QBO_a amplitude (Figures 28b and 28c) shows three prominent peaks in the region 18–22 km, 23– 27 km and 28–32 km with peak amplitude centered around 20 km, 25 km and 30 km, respectively. This feature is remarkably symmetric about the. equator, in both the hemispheres. Another interesting feature to be noted is that the phase remains fairly constant around these peaks. In the equatorial region, the phase of QBO_a around 25 km is ~15 months and that at around 30 km and 20 km are ~28 and 0 months, respectively. Thus the phase difference of QBO_a in the upper and lower regime with respect to that at 25 km is around 13 and 15 months, which corresponds to 156° and 180°, respectively (for the 30 month periodicity one month in phase corresponds to 12°). This shows that the QBO_a around 25 km is almost out of phase with that in the upper (28–32 km) and lower (18–22 km) regime [88].

Over the off-equatorial region the altitude structure of the amplitude and phase of QBO_a are found to be different from that over the equatorial region. Figures 28a and 28d show that the

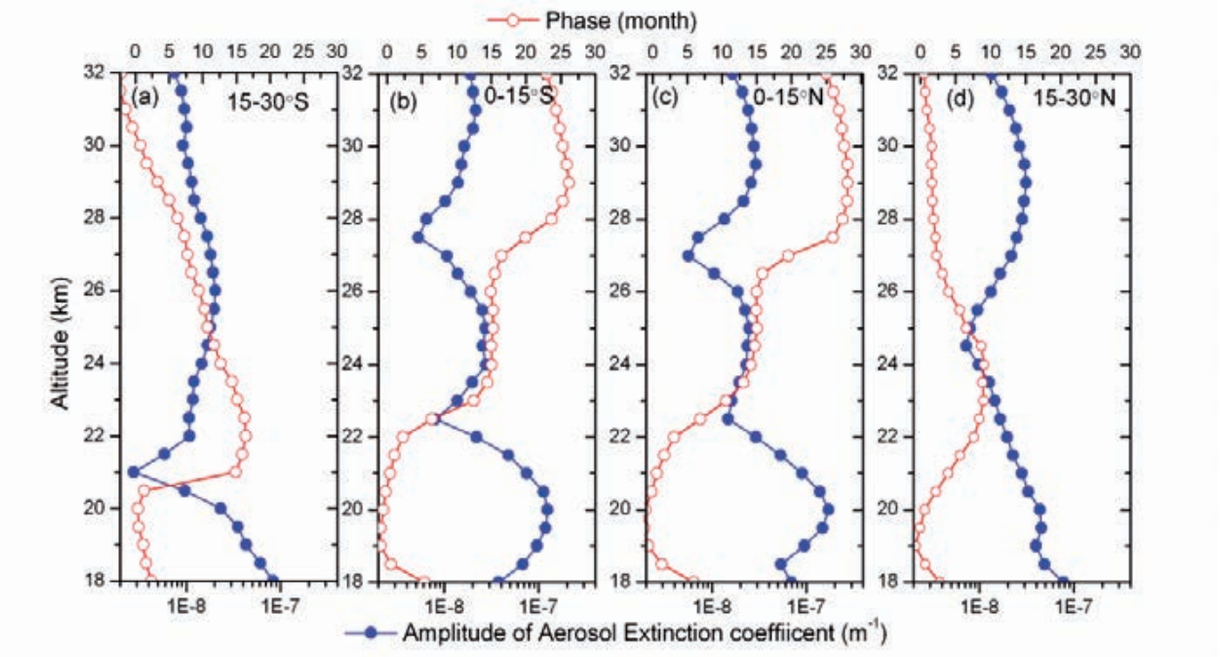

Figure 28. Altitude structure of the QBO amplitude and phase in aerosol extinction for the altitude region 18–32 km in the equatorial region [(c) 0°N–15°N and (b) 0°S–15°S] and off-equatorial region [(d) 15°N–30°N and (a) 15°S–30°S].

amplitude of QBO_a is significant in the lower and upper altitude regions with a minimum value around 24.5 km in the northern hemisphere and around 21 km in the southern hemisphere. While the amplitude of QBO_a shows a broad maximum in the altitude region 24–28 km with a peak around 26 km in the southern part, correspondingly it shows a maximum around 29 km in the northern part.

Over the equatorial region, the observed features of QBO_a in the three altitude regions could be attributed to the influence of the secondary meridional circulation (SMC) induced by the vertical shear of QBO in stratospheric zonal wind. Through a detailed analysis of the QBO modulation of the meridional wind in the stratosphere, Ribera et al. [87] demonstrated the existence of discrete zones of meridional wind convergence and divergence over the equator. These convergence (divergence) zones during the westerly (easterly) phase of QBO_U are located at the lower and upper limits of the maximum zonal wind shear and maximum temperature anomaly layers. The existence of convergence and divergence zones, which are directly related to the rising and sinking motions, forms two circulation cells (SMC) in the consecutive vertical levels, quasi-symmetric about the equator.

To examine the cycle-to-cycle variation of the QBO in aerosol extinction coefficient and its phase structure at the three altitude regions, the monthly mean values of α_p at the central altitudes (of the three regions) 20 km, 25 km and 30 km for the equatorial region 0–15°N and 0–15°S are estimated during the period 1998 to 2005 and this data is subjected to wavelet analysis (after de-trending). Contour plots in Figure 29 shows the time history of the

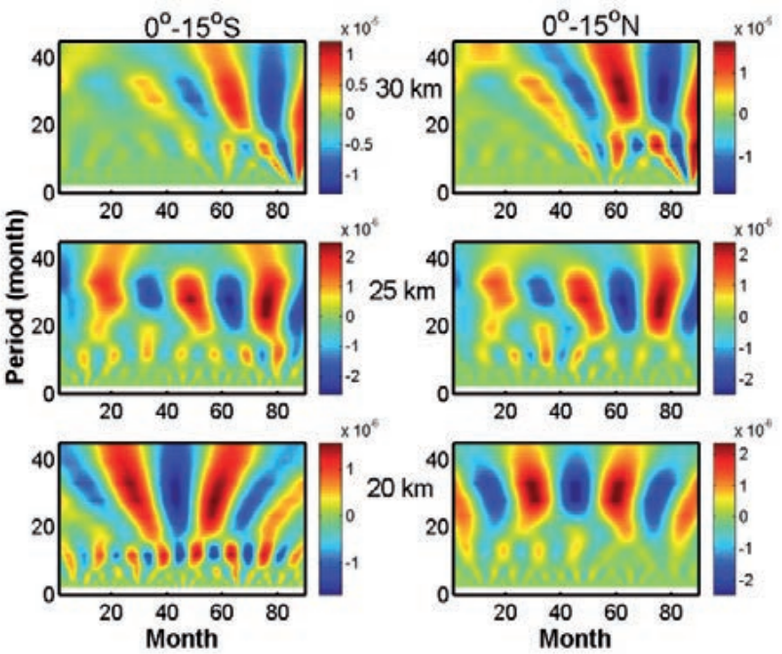

Figure 29. Wavelet spectra of zonal averaged monthly mean aerosol extinction at 20, 25, and 30 km for the equatorial region 0°N–15°N and 0°S–15°S during the period 1998–2005.

amplitudes for different periodicities (ranging from 2 to 45 months) in α_p for the study period. The spectral characteristics at the respective altitudes are similar in both the hemispheres. The annual component repeats coherently in all the three altitudes indicating that they follow the same pattern in the entire altitude range 18–32 km. But the temporal pattern of QBO differs. When the QBO in α_p is in its positive phase (maximum amplitude) in the lower (20 km) and upper (30 km) regimes, it is in the negative phase (minimum amplitude) in the middle regime (25 km). The QBO_a at 25 km is out of phase with that in the upper and lower regimes during the entire study period. However, the amplitudes of AO and QBO in α_p at 30 km are relatively small in the first 40 months compared to rest of the period. This analysis confirms the temporal repeatability of QBO_a phase structure in these three altitude regions inferred from the mean α_p at different altitudes averaged for the entire period of analysis shown in Figure 28. The phase of QBO_U (Figure 23) matches with that of QBO_a in the middle regime (25 km) while it is in opposite phase with those in the lower (20 km) and upper (30 km) regime.

Studies by Fadnavis and Beig [96] on the influence of SMC induced by QBO in the spatiotemporal variations of ozone over the tropical and subtropical regions however showed maximum amplitude of the QBO signal in ozone concentration at the two pressure levels, 30 hPa and 9 hPa, where the QBO manifests in opposite phase. This feature is in good agreement with the amplitude and phase of the QBO signal observed in aerosol extinction coefficient at 25 km and 30 km. From Figures 28b and 28c it can be seen that while the maximum amplitude of QBO signal in aerosol extinction coefficient centered around 20 and 30 km coincides with SMC cells centered at ~80 hPa and ~9 hPa as illustrated by Plumb and Bell [98] and Punge et al. [99], the maximum QBO signal in aerosol extinction coefficient in the altitude region 23–27 km centered around 25 km coincides with the level of maximum zonal wind shear (centered ~24 hPa) where the divergence and convergence zones (circulation cells) intersect. Similarly, Dunkerton [100] studied the QBO anomalies in ozone, methane and water vapor and observed a double peak structure in their amplitudes. Numerical simulations of QBO anomalies also showed influence of SMC in modulating the distribution of tracers leading to the formation of two peaks in their number density near 24 and 32 km [101-103]. However, the observed maximum amplitude of QBO in α_p centered around 20 km is not reproduced in these model simulations.

18. Summary

The altitude structure of aerosol extinction in the tropical UTLS region and its variability in different time scales is examined with particular stress for the Indian longitude sector, using the data from a dual polarization lidar (at 532 nm wavelength) located at Gadanki along with data obtained from SAGE-II onboard ERBS. Organized convection associated with the Asian summer monsoon (ASM) and highly dynamic ITCZ makes this region unique in the global scenario. Altitude profiles of particulate extinction for a period of eight years from 1998-2005 (volcanically quiescent period) obtained from SAGE-II in the latitude region 30°S

to 30°N and the altitude profiles of particulate backscatter, particulate extinction and volume depolarization for the same period derived from lidar data at Gadanki are used for this purpose. The lidar data are used mainly to study the influence of local features such as STCs, local convection etc in the properties of particulates in the UTLS region while the satellite data are used to study the spatial features in the tropical UTLS from 30°S to 30°N. A comparison of aerosol extinction from SAGE-II with that from lidar on a profile basis as well as on monthly mean basis over a small geographical grid size (6° in latitude and 13° in longitude) centered at Gadanki showed a very good agreement between the two in the major features such as mean altitude structure as well as the mean annual pattern.

Lidar studies show a significant increase is particulate scattering in the upper troposphere with a high value of δ over the Indian subcontinent during the ASM period when the tropospheric convective activity is the highest. This feature is clearly associated with particle formation due to homogenous/heterogeneous nucleation and condensation and subsequent freezing to form non-spherical ice crystals (associated with STC). The particulate backscatter coefficient in the LS region is maximum during winter and minimum during the ASM period. The winter peak is closely associated with the increase in vertical mass flux in conjunction with the tropical upwelling and Brewer Dobson circulation.

Occurrence of STCs in the UT region is very common in this geographical region. The frequency of occurrence of STC is the largest during the ASM period, when most of the observed STCs are optically dense and geometrically thick. The most favoured altitude for STC is 14-16 km. Most of the observed STCs are optically and geometrically thin. Thin STCs are generally observed at higher altitudes, very close to the cold point. Most of the dense STCs are found to be associated with organized convection while the thin STCs could be of *in situ* origin. The values of δ in these clouds vary from 0.03 to 0.6 with low values occurring more frequently than high values. Though cloud depth (thickness) generally varies from 0.4 to ~4.0 km, in majority of the cases it is less than 1.7 km. While the cloud optical depth, in general, increases with increase in cloud temperature, the depolarization shows a decrease. For values of temperature < 198 K, the cloud thickness and depolarization show a sharp decrease. These clouds contribute significantly to the particulate scattering in the UT region. High value of β_P observed in the UT region during the ASM period is mainly contributed by the STC particulates. They also contribute to scattering in the lower stratosphere, very close to the cold point, mainly through the penetration of particles from these STCs across the tropopause aided by the upward propagating inertia-gravity waves. This feature, which is characteristic for the Indian monsoon region, is almost absent in the southern hemisphere where the occurrence of organized very deep convection is minimal. However, the Brewer-Dobson circulation plays a significant role in the transport of UT particles in to the lower stratosphere during the winter season.

The convective activity prevailing in the troposphere significantly influences the microphysical properties of particulates in the UTLS region. The particulate scattering and optical depth in the UT region shows a general decrease with increase in latitude on either

side of the equator with a well pronounced summer-winter contrast. However, organized convection during the ASM period enhances the particulate loading in the UT in the northern latitudes even beyond 25°N. While the particulate optical depth in the 18–21 km region (lowest part of the stratosphere) is relatively low in the equatorial region, it shows an increase in the off-equatorial region mainly due to this enhancement in particulate concentration above the cold point, particularly over the Indo-Gangetic Plain, during this period. At a higher altitude (21–30 km) it shows a different pattern, with high values near the equator and low values in the off-equatorial region. This confirms the existence of a stratospheric aerosol reservoir. This spatial distribution could be attributed to horizontal advection in the lower regime (rapid transport from near equatorial region to higher latitudes) as well as lofting to higher altitudes over the equatorial region (B-D circulation).

Spectral analysis of zonal mean particulate optical depth in the stratosphere (18-32km) revealed the existence of a strong QBO both in the equatorial and off-equatorial regions. The phase of the QBO signal in particulate extinction (QBO_a) around 25 km is found to be in opposite phase with that in the upper (28-32 km) and lower regime (18-22 km), illustrating the existence of a secondary meridional circulation (SMC) produced due to vertical shear of QBO phase in zonal wind (QBO_U). While the particulate optical depth in the lower stratosphere is relatively large during the westerly phase of QBO_U in the equatorial region, relatively high values are observed during the easterly phase of QBO_U in the off-equatorial region. During the westerly phase of stratospheric QBO_U, the mean particulate optical depth rapidly decreases with increase in latitude on either side of equator in both the hemispheres. During the easterly phase, this remains fairly steady between ±15° latitude, with a small bite-out around the equator, and decreases steadily for latitudes beyond 15°.

Author details

S.V. Sunilkumar and K. Parameswaran
Space Physics Laboratory, Vikram Sarabhai Space Centre, Thiruvananthapuram, India

Bijoy V. Thampi
Laboratoire de Météorologie Dynamique, IPSL, Place Jussieu, Paris, France

Acknowledgement

We thank the NASA Langley Research Center (NASA-LaRC) and the NASA Langley Aerosol Research Branch for providing the SAGE-II data through the web site ftp://ftp-rab.larc.nasa.gov/pub/sage2/v6.20. The authors are thankful to the technical and scientific staff of National Atmospheric Research Laboratory (NARL), Gadanki for their dedicated efforts in conducting the Lidar observations. One of the authors, Dr. K. Parameswaran would like to acknowledge CSIR for providing grant through the Emeritus Scientist scheme.

19. References

[1] Jensen EJ, Toon OB, Pfister L, Selkirk, HB. Dehydration of the upper troposphere and lower stratosphere by subvisible cirrus clouds near the tropical Tropopause. Geophysical Research Letter 1996;23 825-828.

[2] Luo BP, et al. Dehydration potential of ultrathin clouds at the tropical Tropopause. Geophysical Research Letter 2003;30(11) 1557 doi:10.1029/2002GL016737.

[3] Hartmann DL. Holton JR, Fu Q. The heat balance of the tropical tropopause, cirrus, and stratospheric Dehydration. Geophysical Research Letters 2001;28(10) 1969–1972.

[4] Riese M, Friedl-Vallon F, Spang R, Preusse P, Schiller C, Hoffmann L, Konopka P, Oelhaf H, von Clarmann Th., Höpfner M. GLObal limb Radiance imager for the atmosphere (GLORIA): scientific objectives. Advances in Space Research 2005;36, 989–995.

[5] Froyd KD, Murphy DM, Sanford TJ, Thomson DS, Wilson JC, Pfister L, Lait L. Aerosol composition of the tropical upper troposphere, Atmospheric Chemistry and Physics 2009;9 4363-4385.

[6] de Reus M, Borrmann S, Bansemer A, Heymsfield AJ, Weigel R, Schiller C, Mitev V, Frey W, Kunkel D, Kürten A, Curtius J, Sitnikoev NM, Ulanovsky A, Ravegnani F. Evidence for ice particles in the tropical stratosphere from in-situ measurements. Atmospheric Chemistry and Physics 2009;9, 6775–6792.

[7] Thampi BV, Sunilkumar SV, Parameswaran K. Lidar studies of particulates in the UTLS region at a tropical station over the Indian subcontinent. Journal of Geophysical Resarch 2009 ;114, D08204, doi:10.1029/2008JD010556.

[8] McFarquhar GM, Heymsfield AJ, Pinhirne J, Hart B. Thin and subvisual tropopause tropical cirrus: Observations and Radiative Impacts. Journal of Atmospheric Sciences 2000;57, 1841-1853.

[9] Haladay T, Stephens G. Characteristics of tropical thin cirrus clouds deduced from joint CloudSat and CALIPSO observations. Journal of Geophysical Research 2009;114, D00A25, doi:10.1029/2008JD010675.

[10] Sato M, Hansen J, McCormick M, Pollack J. Stratospheric Aerosol Optical Depths 1850–1990. Journal of Geophysical Research 1993;98(D12), 22,987-22,994.

[11] Barnes JE, Hofmann DJ. Variability in the stratospheric background aerosol over Mauna Loa Observatory. Geophysical Research Letter 2001;28, 2895–2898.

[12] Jäger H. Long-term record of lidar observations of the stratospheric aerosol layer at Garmisch-Partenkirchen. Journal of Geophysical Research 2005;110, D08106, doi:10.1029/2004JD005506.

[13] Deshler T, Anderson-Sprecher R, Jäger H, Barnes JE, Hofmann DJ, et al. Trends in the nonvolcanic component of stratospheric aerosol over the period 1971-2004. Journal of Geophysical Research 2006;111, D01201, doi:10.1029/2005JD006089.

[14] Grant WB et al. Aerosol-associated changes in tropical stratospheric ozone following the eruption of Mount Pinatubo. Journal of Geophysical Research 1992;99, 8197-8211.

[15] Angell JK, Korshover J, Planet WG. Ground-based and satellite evidence for a pronounced total-ozone minimum in early 1983 and responsible atmospheric layers. MonthlyWeather Review 1985;113, 641-646.

[16] Hofmann DJ, Solomon S. Ozone destruction through heterogeneous chemistry following the eruption of El Chichón. Journal of Geophysical Research 1989;94, 5029-5041.

[17] Deshler T, Johnson BJ, Hofmann DJ, Nardi B. Correlations between ozone loss and volcanic aerosol at latitudes below 14 km over McMurdo Station, Antarctica. Geophysical Research Letter 1996;23, 2931–2934, doi:10.1029/96GL02819.

[18] Koike M, Kondo Y, Matthews WA, Johnston PV, Yamazaki K. Decrease of stratospheric NO_2 at 44°N caused by Pinatubo volcanic aerosols. Geophysical Research Letter 1993;20(18), 1975-1978.

[19] Coffey MT, Mankin WG. Observations of the loss of stratospheric NO2 following volcanic eruptions. Geophysical Research Letter 1993;20(24), 2873-2876.

[20] Johnston PV, McKenzie RL, Keys JG, Matthews WA. Observations of depleted stratospheric NO2 following the Pinatubo volcanic eruption. *Geophysical Research Letter* 1992;*19*, 211- 213.

[21] McCormick MP, Thomason LW, Trepte CR. Atmospheric effects of the MtPinatubo eruption. *Nature* 1995;*373*, 399-404.

[22] Thomason LW, Burton SP, Luo BP, Peter T. SAGE II measurements of stratospheric aerosol properties at non-volcanic levels. Atmospheric Chemistry and Physics 2008;8, 983–995.

[23] Thomason LW, Kent GS, Trepte CR, Poole LR. A comparison of the stratospheric aerosol background periods of 1979 and 1989–1991. Journal of Geophysical Research 1997;102, 3611-3616.

[24] Thomason LW, Peter T., editors. Assessment of stratospheric aerosol properties (ASAP). SPARC Report 4; 2006. WMO/TD 1295, Technical Report 2006 WCRP-124, World Climate Research Program, Geneva, Switzerland.

[25] Deshler T, Hervig ME, Hofmann DJ, Rosen JM, Liley JB. Thirty years of in situ stratospheric aerosol size distribution measurements from Laramie, Wyoming (41°N), using balloon-borne instruments. Journal of Geophysical Research 2003;108(D5), 4167, doi:10.1029/2002JD002514.

[26] Hofmann DJ, Barnes JE, O'Neill M, Rudeau MT, Neely R. Increase in background stratospheric aerosol observed with lidar at Mauna Loa Observatory and Boulder, Colorado. Geophysical Research Letter 2009;36, L15808, doi:10.1029/2009GL039008.

[27] Graf H.-F, Langmann B, Feichter J. The contribution of Earth degassing to the atmospheric sulfur budget. Chem Geol. 1998;147, 131-145.

[28] Trepte CR, Hitchman MH. Tropical stratospheric circulation deduced from satellite aerosol data. Nature 1992;355, 626–628, doi:10.1038/355626a0.

[29] Hitchman MH, Mckay M, Trepte CR. A climatology of stratospheric aerosol. Journal of Geophysical Research 1994;99(D10), 20,689-20,700.

[30] Choi W, Grant W, Park J, Lee KM, Lee H, Russell III J. Role of the quasi-biennial oscillation in the transport of aerosols from the tropical stratospheric reservoir to midlatitudes. Journal of Geophysical Resresearch 1998;103(D6), 6033-6042.

[31] Barnes JE, Hofmann DJ. Lidar measurements of stratospheric aerosol over Mauna Loa. Geophysical Research Letter 1997;24, 1923–1926.

[32] McCormick MP. SAGE II: An overview. Advances in Space Research 1987;7(3), 219–226.

[33] Mauldin III LE, Zaun NH, McCormick MP, Guy JH, Vaughan WR. Stratospheric Aerosol and Gas Experiment II instrument: A functional description. Optical Engineering 1985;24, 307–312.

[34] Chu WP, McCormick MP, Lenoble J, Brogniez C, Pruvost P. SAGE II inversion algorithm. Journal of Geophysical Research 1989;94(D6), 8339–8351.

[35] Wang P-H, McCormick MP, Minnis P, Kent GS, Yue GK, Skeens KM. A method for estimating vertical distribution of the SAGE II opaque cloud frequency. Geophysical Research Letter 1995;22(3), 243–246.

[36] Wang P-H, Minnis P, McCormick MP, Kent GS, Skeens KM. A 6-year climatology of cloud occurrence frequency from Stratospheric Aerosol and Gas Experiment II observations (1985–1990). Journal of Geophysical Research 1996;101(D23), 29,407–29,429.

[37] Sunilkumar SV, Parameswaran K, Krishna Murthy BV. Lidar observations of cirrus cloud near the tropical tropopause: General features. Atmospheric Research 2003;66, 203-227.

[38] Sunilkumar SV, Parameswaran K. Temperature dependence of tropical cirrus properties and radiative effects. Journal of Geophysical Research 2005;110, D13205, doi:10.1029/2004JD005426.

[39] Parameswaran K, Thampi BV, Sunilkumar SV. Latitudinal dependence of the seasonal variation of particulate extinction in the UTLS over the Indian longitude sector during volcanically quiescent period based on lidar and SAGE-II observations. Journal of Atmospheric and Solar Terrestrial Physics 2010;72, 1024-1035.

[40] Fernald, FG. Analysis of atmospheric lidar observations: Some comments. Applied Optics 1984;23, 652– 653, doi:10.1364/AO.23.000652.

[41] Bodhaine BA, Wood BN, Dutton EG, Slusser JR. On Rayleigh optical depth calculations. *Journal of Atmosphere and OceanTechnology* 1999;16, 1854-1861.

[42] Sunilkumar SV, Parameswaran K, Thampi BV, Interdependence of tropical cirrus properties and their variability. Annales Geophysicae 2008;26, 413-429.

[43] Pfister et al.Aircraft observations of thin cirrus clouds near the tropical Tropopause. *Journal of Geophysical Research* 2008;106(D9), 9765-9786.

[44] Garrett TJ, Zulauf MA, Krueger SK. Effects of cirrus near the tropopause on anvil cirrus dynamics. *Geophysical Research Letter* 2006;*33*, L17804, doi:10.1029/2006GL027071.

[45] Chen JP, McFarquhar GM, Heymsfield AJ, Ramanathan V. A modeling and observational study of the detailed microphysical structure of tropical cirrus anvils. Journal Geophysics Research 1997;102(D6), 6637-6653.

[46] Sassen K, Cho BS. Subvisual thin cirrus lidar data set for satellite verification and climatological research. Journal of Applied Meteorology 1992 ;31, 1275-1285.

[47] Yue GK, Fromm MD, Shettle EP. Intercomparison of aerosol extinction measured by Stratospheric Aerosol and Gas Experiment (SAGE) II and III. Journal of Geophysical Research 2009;114, D07205, doi:10.1029/2008JD010452.

[48] Antuna JC, Robock A, Stenchikov GL, Thomason LW, Barnes JE. Lidar validation of SAGE II aerosol measurements after the 1991 Mount Pinatubo eruption. Journal of Geophysical Research 2002;107 (D14), 4194. doi:10.1029/2001JD001441.

[49] Lu J, Mohnen VA, Yue GK, Jäger H. Intercomparison of multiplatform stratospheric aerosol and ozone observations. Journal of Geophysical Research 1997;102 (D13), 16,127–16,136.

[50] Lu C-H, Yue GK, Manney GL, Jäger H, Mohnen VA. Lagrangian approach for stratospheric aerosol and gas experiment (SAGE) II profile intercomparisons. Journal of Geophysical Research 2000;105, 4563–4572.

[51] Winker DM, Trepte CR. Laminar cirrus observed near the tropical tropopause by LITE. Geophysical Research Letter 1998;25, 3351-3354.

[52] Mergenthaler JL, Roche AE, Kumer JB, Ely GA. Cryogenic limb array etalon spectrometer observations of tropical cirrus. Journal Geophysical Res 1999;104, 22183-22194.

[53] Massie ST, Lowe P, Tie X, Hervig M, Thomas G, Russell J. Effect of the 1997 El Nino on the distribution of upper tropospheric cirrus. Journal of Geophysical Research 2000;105, 22725-22741.

[54] Roca R, Viollier M, Picon L, Desbois M. A multisatellite analysis of deep convection and its moist environment over the Indian Ocean during the winter monsoon. Journal of Geophysical Research 2002;107(D19), 8012, doi:10.1029/2000JD000040.

[55] Rajeev K, Parameswaran K, Meenu S, Sunilkumar SV, Thampi BV, Suresh Raju C, Krishna Murthy BV, Jagannath KS, Mehta SK, Narayana Rao D, Rao KG. Observational assessment of the potential of satellite-based water vapor and thermal IR brightness temperatures in detecting semitransparent cirrus. Geophysical Research Letter 2008;35, L08808, doi:10.1029/2008GL033393.

[56] Heymsfield AJ, McFarquhar GM. Mid-latitude and tropical cirrus-Microphysical properties. In: Lynch D, Sassen K, Starr DO, Stephens G. (eds.) Cirrus. Oxford University Press;2002. p78-101.

[57] Sassen K. The lidar backscatter depolarization technique for cloud and aerosol research. In Mishenko ML, Hovenier JW, Travis LD. (eds.) *Light Scattering by Nonspherical Particles: Theory, Measurements and Geophysical Applications*. Academic Press, New York; 2000.pp393-416.

[58] Noel V, Winker DM, McGill M, Lawson P. Classification of particle shapes from lidar depolarization ratio in convective ice clouds compared to in situ observations during CRYSTAL-FACE. *Journal of Geophysical Research* 2004;*109*, D24213, doi:10.1029/2004JD004883.

[59] Roca R, Ramanathan V. Scale dependence of monsoonal convective systems over the Indian Ocean. *Journal of Climate* 2000;*13*, 1286-1297.

[60] Wong S, Dessler AE. Regulation of H_2O and CO in tropical tropopause layer by the Madden-Julian oscillation. *Journal of Geophysical Research* 2007;*112*, D14305, doi:10.1029/2006JD007940.

[61] Gettelman A, Seidel DJ, Wheeler MC, Ross RJ. Multi-decadal trends in tropical convective available potential energy. *Journal of Geophysical Research* 2002;*107*(D21), 4606, doi:10.1029/2001JD001082.

[62] Stull RB. *Meteorology Today for Scientists and Engineers.* West publishing company, StPaul, Minneapolis; 1995.

[63] Manohar G, Kandalgaonkar S, Tinmaker M. Thunderstorm activity over India and the Indian southwest monsoon. *Journal of Geophysical Research* 1999;*104*(D4), 4169-4188.

[64] Haynes PH, McIntyre ME, Shepherd TG, Marks CJ, Shine KP. On the ''downward control'' of extratropical diabatic circulations by eddy-induced mean zonal forces. *Journal of Atmospheric Sciences* 1991;48, 651-678, doi:10.1175/1520-0469.

[65] Holton JR, Haynes PH, McIntyre ME, Douglass AR, Rood RB, Pfister L. Stratosphere-troposphere exchange. Review of Geophysics 1995;33, 403-439.

[66] Yulaeva E, HoltonJR, Wallace JM. On the cause of the annual cycle in tropical lower stratospheric temperatures. *Journal of Atmospheric Sciences*1994;*51*, 169-174.

[67] Reid GC, Gage KS. On the annual variation of height of the tropical Tropopause. *Journal of Atmospheric Sciences* 1981;38, 1928– 1937.

[68] Krishna Murthy BV, Parameswaran K, Rose KO. Temporal variations of the tropical tropopause characteristics. Journal of Atmospheric Sciences 1986;43:914–923.

[69] Highwood EJ, Hoskins BJ. The tropical Tropopause. *Quarterly Journal of Royal Meteorological Society* 1998;*124*, 1579-1604.

[70] Seidel DJ, Ross RJ, Angell JK, Reid GC. Climatological characteristics of the tropical tropopause as revealed by radiosondes. *Journal of Geophysical Research* 2001;106(D8), 7857-7878.

[71] Staley D. On the mechanism of mass and radioactivity transport from stratosphere to troposphere. *Journal of Atmospheric Sciences* 1962;*19*(6), 450-467.

[72] Reiter ER, Glasser ME, Mahlman JD. The role of the tropopause in the stratospheric-tropospheric exchange process. *Pure Applied Geophysics* 1969;75, 185-218.

[73] Reiter ER. Stratospheric-tropospheric exchange processes. *Review of Geophysics and Space Physics* 1975;*13*(4), 459-474.

[74] Rosenlof KH, Tuck AF, Kelly KK, Russell III JM, McCormick MP. Hemispheric asymmetries in water vapor and inferences about transport in the lower stratosphere. *Journal of Geophysics Research* 1997;*102*, 13,213-13,234.

[75] Dessler AE. The effect of deep, tropical convection on the tropical tropopause layer. *Journal of Geophysical Research* 2002;*107*(D3), 4033, doi:10.1029/2001JD000511.

[76] Gettelman A, Kinnison DE, Dunkerton TJ, Brasseur GP. Impact of monsoon circulations on the upper troposphere and lower stratosphere. *Journal of Geophysical Research* 2004;*109*, D22101, doi:10.1029/ 2004JD004878.

[77] Park M, Randel WJ, Kinnison DE, Garcia RR, Choi W. Seasonal variation of methane, water vapor, and nitrogen oxides near the tropopause: Satellite observations and model simulations. *Journal of Geophysical Research* 2004;*109*, D03302, doi:10.1029/2003JD003706.

[78] Sunilkumar, SV, Parameswaran K, Rajeev K, Krishna Murthy BV, Meenu S, Mehta SK, Asha Babu. Semitransparent Cirrus clouds in the Tropical Tropopause Layer during two contrasting seasons. Journal of Atmospheric and Solar Terrestrial Physics 2010; 72,745-762,doi:10.1016/j.jastp.2010.03.020.

[79] Das SS, Kumar KK, Uma KN. MST radar investigation on inertia-gravity waves associated with tropical depression in the upper troposphere and lower stratosphere over Gadanki (13.5°N, 79.2°E). Journal of Atmospheric and Solar Terrestrial Physics 2010;72, 1184-1194, doi:10.1016/j.jastp2010.07.016.

[80] Thampi BV, Parameswaran K, Sunilkumar SV. Semitransparent cirrus clouds in the upper troposhere and their contribution to the particulate scattering in the tropical UTLS region. Journal of Atmospheric and Solar Terrestrial Physics 2012;74,1-10, doi:10.1016/j.jastp2011.09.005.

[81] Meenu S, Rajeev K, Parameswaran K, Nair AKM. Regional distribution of deep clouds and cloud top altitudes over the Indian subcontinent and the surrounding oceans. Journal of Geophysical Research 2010 ;115, D05205, doi:10.1029/2009JD011802.

[82] Yue GK, McCormick MP, Chiou EW. Stratospheric aerosol optical depth observed by the Stratospheric Aerosol and Gas Experiment II: Decay of the El Chichon and Ruiz volcanic perturbations. Journal of Geophysical Research 1991;96(D3), 5209–5219.

[83] Trepte, C.R., Thomason, L.W., Kent, G.S. Banded structures in stratospheric aerosol distributions. Geophysical Research Letters 1994; 21 (22), 2397–2400

[84] Bauman JJ, Russell PB, Geller MA, Hamill P. A stratospheric aerosol climatology from SAGE II and CLAES measurements: 2Results and comparisons, 1984-1999. *Journal of Geophysical Research* 2003;*108 (D13)*, 4383, doi:10.1029/2002JD002993.

[85] Junge CE, Changnon CW, Manson JE. Stratospheric aerosols. *Journal of Meteorology* 1961;*18*, 81-108.

[86] Robock A. Volcanic eruptions and climate. Review of Geophysics 2000;38, 191-219.

[87] Parameswaran K, Sunilkumar SV, Krishna Murthy BV, Satheesan K, Bhavanikumar Y, Krishnaiah M, Nair PR. Lidar Observations of cirrus cloud near the tropical tropopause: temporal variations and association with tropospheric turbulence. *Atmospheric Research* 2003;*69*, 29-49.

[88] Sunilkumar SV, Parameswaran K, Thampi BV, Ramkumar G. Variability in background stratospheric aerosols over the tropics and its association with atmospheric dynamics. *Journal of Geophysical Research* 2011;116, D13204, doi:10.1029/2010JD015213.

[89] Newhall CG, Self S. The volcanic explosivity index (VEI): An estimate of explosive magnitude for historical volcanism. Journal of Geophysical Research 1982 ;87,1231–1238.

[90] Hamill P, Jensen EJ, Russell PB, Bauman JJ. The life cycle of stratospheric aerosol particles. Bulletin of American Meteorological Society 1997;7, 1395–1410.

[91] Rosen JM. The boiling point of stratospheric aerosol. Journal of Applied Meteorology 1971;18, 1044-1046.

[92] Deshler T. A review of global stratospheric aerosol: Measurements, importance, life cycle, and local stratospheric aerosol. Atmospheric Research 2008; 90,223-232,doi:10.1016/j.atmosres.2008.03.016.

[93] Randel WJ, Wu F, Voemel H, Nedoluha GE, Forster P. Decreases in stratospheric water vapor after 2001: links to changes in the tropical tropopause and the Brewer-Dobson circulation. Journal of Geophysical Research 2006;111(12), doi:10.1029/2005JD006744.

[94] Randel WJ, Wu F, Oltmans SJ, Rosenlof K, Nedoluha GE. Interannual changes of stratospheric water vapor and correlations with tropical tropopause temperatures. Journal Atmospheric Sciences 2004;61, 2133–2148.

[95] Bingen C, Fussen D, Vanhellemont F. A global climatology of stratospheric aerosol size distribution parameters derived from SAGE II data over the period 1984–2000. Journal of Geophysical Research 2004;109, D06202, doi:10.1029/2003JD003511.

[96] Fadnavis S, Beig G. Spatiotemporal variation of the ozone QBO in MLS data by wavelet analysis. Annales Geophysicae, 2008;26, 3719–3730.

[97] Ribera P, Penã-Ortiz C, Garcia-Herrera R, Gallego D, Gimeno L, Hernàndez E. Detection of the secondary meridional circulation associated with the quasi-qiennial oscillation. Journal of Geophysical Research 2004;109, D18112, doi:10.1029/2003JD004363.

[98] Plumb RA, Bell RC. A model of the quasi-biennial oscillation on equatorial beta plane. Quarterly Journal of Roya; Meteorological Society 1982;108, 335–352.

[99] Punge HJ, Konopka P, Giorgetta MA, Müller R. Effects of the quasi-biennial oscillation on low-latitude transport in the stratosphere derived from trajectory calculations. Journal of Geophysical Research 2009;114, D03102, doi:10.1029/2008JD010518.

[100] Dunkerton TJ. Quasi-biennial and subbiennial variation of stratospheric trace constituents derived from HALOE observations. Journal of Atmospheric Sciences 2001;58, 7–25.

[101] Chipperfield MP, Gray LJ, Kinnersley JS, Zawodny J. A two-dimensional model study of the QBO signal in SAGE-II NO2 and O3. Geophysical Research Letter 1994;21, 589–592.

[102] Jones DBA, Schneider HR, McElroy MB. Effects of the quasi-biennial oscillation on the zonally averaged transport of tracers. Journal of Geophysical Research 1998;103, 11,235–11,249.

[103] McCormack JP, Siskind DE, Hood LL. Solar–QBO interaction and its impact on stratospheric ozone in a zonally averaged photochemical transport model of the middle atmosphere. Journal Geophysical Research 2007;112, D16109.

IntechOpen